Mechanism of critical heat flux during flow boiling of subcooled water in a circular tube at high liquid Reynolds number

Hata, Koichi

Fukuda, Katsuya

Masuzaki, Suguru

(Citation)
Experimental Thermal and Fluid Science,70:255-269

(Issue Date)
2016

(Resource Type)
journal article

(Version)
Accepted Manuscript

(URL)
https://hdl.handle.net/20.500.14094/90003474

Mechanism of Critical Heat Flux during Flow Boiling of Subcooled Water in a Circular Tube at High Liquid Reynolds Number

Koichi Hata

Graduate School of Maritime Sciences, Kobe Univ.

5-1-1, Fukaeminami, Higashinada, Kobe 658-0022, Japan

Email Address hatako1@people.kobe-u.ac.jp

Katsuya Fukuda

Graduate School of Maritime Sciences, Kobe Univ.

5-1-1, Fukaeminami, Higashinada, Kobe 658-0022, Japan

Email Address fukuda@maritime.kobe-u.ac.jp

Suguru Masuzaki

National Institute for Fusion Science

322-6 Oroshi-cho, Toki, Gifu 509-5292, Japan

Email Address masuzaki@LHD.nifs.ac.jp

ABSTRACT

The subcooled boiling heat transfer and the steady state critical heat flux (CHF) in a vertical circular tube for the liquid Reynolds numbers (Re_d=2.77×10^4 to 3.08×10^5) and the flow velocities (u=3.95 to 30.80 m/s) are systematically measured by the experimental water loop comprised of a multistage canned-type circulation pump with high pump head. The SUS304

test tube of inner diameter (d=6 mm) and heated length (L=59.5 mm) is used in this work. The outer surface temperatures of the SUS304 test tube with heating are observed by an infrared thermal imaging camera and a video camera. The subcooled boiling heat transfers for SUS304 test tube are compared with the values calculated from correlations due to other researchers for the subcooled boiling heat transfer. The influence of flow velocity on the subcooled boiling heat transfer and the CHF is investigated in detail based on the experimental data. Nucleate boiling surface superheats at the CHF are close to the lower limit of the heterogeneous spontaneous nucleation temperature and the homogeneous spontaneous nucleation temperature. A suggestion as to what the dominant mechanism is for the subcooled flow boiling CHF on the SUS304 circular tube is made at high liquid Reynolds number. On the other hand, the RANS equations (Reynolds Averaged Navier-Stokes Simulation) with k-ε turbulent model in a circular tube of a 3 mm in diameter and a 526 mm long are numerically solved for heating of water on heated section of a 3 mm in diameter and a 67 mm long with various thicknesses of conductive sub-layer by using PHOENICS code under the same conditions as the experimental ones previously obtained and with temperature dependent thermo-physical fluid properties. The Platinum (Pt) test tube of inner diameter (d=3 mm) and heated length (L=66.5 mm) was used in this experiment. The thicknesses of conductive sub-layer from non-boiling regime to CHF are measured. The thicknesses of conductive sub-layer at the CHF point are predicted for various flow velocities. The experimental values of the CHF are also compared with the corresponding theoretical values of the liquid sub-layer dry-out models suggested by other researchers, respectively. A suggestion as to what the dominant mechanism is for the subcooled flow boiling CHF on the Pt circular tube is made at high liquid Reynolds number.

KEYWORDS

Mechanisms of Subcooled Flow Boiling, Critical Heat Flux, Vertical Circular Tube, High Liquid Reynolds Number

1. INTRODUCTION

The knowledge of subcooled boiling heat transfer at high liquid Reynolds number is important to discuss the mechanisms of subcooled flow boiling critical heat flux (CHF) in a vertical circular tube. Many researchers have experimentally studied the steady state CHFs uniformly heated on the normal tubes by a steadily increasing current for high liquid Reynolds number and given the correlations for calculating CHFs on the normal tubes. The authors have assumed that flow velocity will affect the incipient boiling superheat and the nucleate boiling heat transfer up to the CHF. Incipient boiling superheat may shift to a very high value at higher flow velocity and a direct transition to film boiling or a trend of a decrease in CHF with an increase in the flow velocity may occur due to the heterogeneous spontaneous nucleation. The accurate measurement for the subcooled boiling heat transfer up to the CHF is necessary to clarify a change in the mechanism of CHF.

The authors have systematically measured the subcooled boiling heat transfer and the steady state critical heat fluxes in a short vertical SUS304-tube for the flow velocities (u=17.2 to 42.4 m/s), the inlet liquid temperatures (T_{in}=293.3 to 362.5 K), the inlet pressures (P_{in}=812.1 to 1467.9 kPa) and the exponentially increasing heat input ($Q=Q_0\ exp(t/\tau)$, τ=8.5 s) by the experimental water loop comprised of a multistage canned-type circulation pump with high

pump head [1, 2]. The SUS304 test tubes of inner diameters (d=3 and 6 mm), heated lengths (L=33 and 59.5 mm), effective lengths (L_{eff}=23.3 and 49.1 mm), L/d (=11 and 9.92), L_{eff}/d (=7.77 and 8.18), and wall thickness (δ=0.5 mm) with average surface roughness (Ra=3.18 μm) were used in this work.

Outlet subcooling:

$$Bo_{cr} = 0.082 D^{*-0.1} We^{-0.3} \left(\frac{L}{d}\right)^{-0.1} Sc^{0.7} \qquad \text{for } \Delta T_{sub,out} \geq 30 \text{ K and } u \leq 13.3 \text{ m/s} \qquad (1)$$

$$Bo_{cr} = 0.0523 D^{*-0.15} We^{-0.25} \left(\frac{L}{d}\right)^{-0.1} Sc^{0.7} \qquad \text{for } \Delta T_{sub,out} \geq 30 \text{ K and } u > 13.3 \text{ m/s} \qquad (2)$$

Inlet subcooling:

$$Bo_{cr} = C_1 D^{*-0.1} We^{-0.3} \left(\frac{L}{d}\right)^{-0.1} e^{-\frac{(L/d)}{C_2 Re_d^{0.4}}} Sc^{*C_3} \qquad \text{for } \Delta T_{sub,in} \geq 40 \text{ K and } u \leq 13.3 \text{ m/s} \qquad (3)$$

$$Bo_{cr} = C_4 D^{*-0.15} We^{-0.25} \left(\frac{L}{d}\right)^{-0.1} e^{-\frac{(L/d)}{C_5 Re_d^{0.5}}} Sc^{*C_6} \qquad \text{for } \Delta T_{sub,in} \geq 40 \text{ K and } u > 13.3 \text{ m/s} \qquad (4)$$

where C_1=0.082, C_2=0.53 and C_3=0.7 for L/d≤around 40 and C_1=0.092, C_2=0.85 and C_3=0.9 for L/d>around 40. C_4=0.0523, C_5=0.144 and C_6=0.7 for L/d≤around 40 and C_4=0.0587, C_5=0.231 and C_6=0.9 for L/d>around 40. Details of the influence of L/d are shown in Appendix A.1 [3]. Bo_{cr}, D^*, We, Sc and Sc^* are boiling number ($=q_{cr,sub}/Gh_{fg}$), non-dimensional diameter [$D^*=d/\{\sigma/g/(\rho_l-\rho_g)\}^{0.5}$], Weber number ($=G^2d/\rho_l\sigma$), non-dimensional outlet subcooling ($=c_{pl}\Delta T_{sub,out}/h_{fg}$) and non-dimensional inlet subcooling ($Sc^*=c_{pl}\Delta T_{sub,in}/h_{fg}$), respectively. Saturated thermo-physical properties were evaluated at the outlet pressure. Most of the data for the exponentially increasing heat input ($Q_0 \exp(t/\tau)$, τ=8.5 to 33.3 s, 3323 points) are within ±15 % differences of Eqs. (1), (2), (3) and (4) for the flow velocities, u, ranging from 4.0 to 42.4 m/s, respectively.

The inner surface temperature and the heat flux for different flow regimes ranging from single-phase flow heat transfer to CHF were explored. The subcooled boiling heat transfers for SUS304 test tube were compared with authors' Platinum test tube data [4] and the values calculated from correlations due to other researchers for the subcooled boiling heat transfer. The influence of flow velocity on the subcooled boiling heat transfer and the CHF was investigated in detail. And the correlation of the subcooled boiling heat transfer for turbulent flow of water in a short vertical SUS304-tube was given based on the experimental data. The precision or accuracy of a more wide set of correlation in predicting the set of data was evaluated [1, 2]. The correlation can describe the subcooled boiling heat transfer coefficients obtained in this work within ±15 % differences. Nucleate boiling surface superheats for the SUS304 test tube become very high. Those at the high flow velocity are close to the lower limit of Heterogeneous Spontaneous Nucleation Temperature [5]. The dominant mechanisms of the flow boiling CHF in a short vertical SUS304-tube were discussed. The CHF occur due to the hydro-dynamic instability suggested by Kutateladze [6] and Zuber [7] or due to the Heterogeneous Spontaneous Nucleation at the lower limit of Heterogeneous Spontaneous Nucleation Temperature.

The objectives of present study are fourfold. First is to measure the subcooled boiling heat transfer and the steady state CHFs for a SUS304-circular test tube with a wide range of inlet subcoolings ($\Delta T_{sub,in}$) and flow velocities (u) at high liquid Reynolds number, while the outer surface temperature of the SUS304-circular test tube with heating is visually observed using an infrared thermal imaging camera and a video camera. Second is to compare the outer surface temperature of the SUS304-circular test tube calculated by the steady one-dimensional heat conduction equation with these cameras' data taken at the same time for the flow velocities ranging from 3.95 to 30.80 m/s. Third is to measure the thicknesses of conductive

sub-layer from non-boiling regime to CHF by numerically analyzing the subcooled flow boiling heat transfer on a Pt-circular test tube of a 3 mm inner diameter previously obtained [4]. Fourth is to make a suggestion based on the experimental data as to what the dominant mechanism is for the subcooled flow boiling critical heat flux on a vertical circular tube at high liquid Reynolds number.

2. EXPERIMENTAL APPARATUS AND METHOD

The schematic diagram of the experimental setup comprised of a water loop and a pressurizer is shown in Fig. 1. The loop is made of SUS304 stainless steel and is capable of working up to 2 MPa. The loop has five test sections whose inner diameters are 2, 3, 6, 9 and 12 mm. Test sections were vertically oriented with water flowing upward. The test section of the inner diameter of 6 mm was used in this work. The circulating water was distilled and deionized with about 20 μS/m specific resistivity. The circulating water through the loop was heated or cooled to keep a desired inlet temperature by pre-heater or cooler. The flow velocity was measured by a mass flow meter using a vibration tube (Nitto Seiko, CLEANFLOW 63FS25, Flow range: 100 to 750 kg/min). The mass velocity was controlled by regulating the frequency of the three-phase alternating power source to the canned type circulation pump (Nikkiso Co., Ltd., Non-Seal Pump Multi-stage Type VNH12-C4 C-3S7SP, pump flow rate=12 m^3/h, pump head=250 m) with an inverter installed a 4-digit LED monitor (Mitsubishi Electric Corp., Inverter, Model-F720-30K). The pump input frequency shows the net pump input power and pump discharge pressure free of slip loss. The water was pressurized by saturated vapor in the pressurizer in this work. The pressure at the outlet of the test tube was controlled within ±1 kPa of a desired value by using a heater controller of the pressurizer.

The cross-sectional view of 6-mm inner diameter test section used in this work is shown in Fig. 2. The SUS304 test tube for the test tube inner diameter, d, of 6 mm, the heated length, L, of 59.5 mm with the commercial finish of inner surface was used in this work. Wall thickness of the test tube, δ, was 0.5 mm. Four fine 0.07-mm diameter platinum wires were spot-welded on the outer surface of the 6 mm inner diameter test tube as potential taps: the first one is at the position of 4.6 mm from the leading edge of the test tube, and the second to forth ones are at 16.5, 16.8 and 15.7 mm from the previous ones, respectively. The effective length, L_{eff}, of the 6 mm inner diameter test tube between the first potential tap and forth one on which average heat transfer was measured was 49.0 mm. The silver-coated 5-mm thickness copper-electrode-plates to supply heating current were soldered to the surfaces of the both ends of the test tube. The both ends of test tube were electrically isolated from the loop by Bakelite plates of 14-mm thickness. The inner surface condition of the test tube was observed by the scanning electron microscope (SEM) photograph (JEOL JXA8600) and inner surface roughness was measured by Tokyo Seimitsu Co., Ltd.'s surface texture measuring instrument (SURFCOM 120A). Figure 3 shows the SEM photograph of the SUS304 test tube for d=6 mm with commercial finish of inner surface. The values of inner surface roughness for *Ra*, *Rmax* and *Rz* were measured 3.89, 21.42 and 15.03 μm, respectively.

The SUS304 test tube has been heated with an exponentially increasing heat input supplied from a direct current source (Takasago Ltd., NL035-500R, DC 35 V-3000 A) through the two copper electrodes shown in Fig. 4. Heat transfer processes caused by exponentially increasing heat inputs, $Q_0 \exp(t/\tau)$, were measured for the SUS304 test tube. The exponential periods, τ, of the heat input ranged from 7.02 to 8.51 s. The common specifications of the direct current source are as follows. Constant-voltage (CV) mode regulation is a 4.75 mV minimum, CV

mode ripple is 500 μV r.m.s. or better and CV mode transient response time is less than 200 μsec (Typical) against 5 % to full range change of load. The transient CHFs, $q_{cr,sub}$, were realized by the exponentially increasing heat input to the test tube. At the CHF, the test tube average temperature rapidly increases. The current for the heat input to the test tube was automatically cut off when the measured average temperature increased up to the preset temperature, which was several degrees (in tens) of Kelvin higher than corresponding CHF surface temperature. This procedure avoided actual burnout of the test tube. Details of the preset temperature are shown in Appendix A.2. The outer surface temperature of the test tube with heating was observed by an infrared thermal imaging camera (NEC Avio Infrared Technologies Co., Ltd. Thermography TVS-200EX) and a video camera (SONY Handycam HDR-CX270V). The accuracy of an infrared thermal imaging camera is ±2 % of reading. The outer surface of the test tube was uniformly painted black with black body spray (Japan Sensor Corporation, JSC-3, emissivity, ε, of 0.94) in this work.

The average temperature, $\overline{T}$, of the SUS304 test tube shown in Fig. 4 was measured with resistance thermometry participating as a branch of a double bridge circuit for the temperature measurement. The output voltages from the bridge circuit, V_T, together with the voltage drop across the potential taps of the test tube (first and forth potential taps, $V_R=IR_T$, first and second ones, $V_{R1}=IR_{T1}$, second and third ones, $V_{R2}=IR_{T2}$, and third and fourth ones, $V_{R3}=IR_{T3}$) and across a standard resistance, $V_I=IR_s$, were amplified and then were sent via an analog-digital (A/D) converter to a digital computer. The unbalance voltage, V_T, is expressed by means of Ohm's low as the following form.

$$V_T = \frac{I\left(R_T \times R_2 - R_1 \times R_3\right)}{R_2 + R_3} \tag{5}$$

These voltages were simultaneously sampled at a constant interval ranging from 60 to 200 ms. The average temperatures of the SUS304 test tube between the first and forth potential taps and between adjacent potential taps (first and second potential taps, second and third ones, and third and fourth ones) were calculated with the aid of previously calibrated resistance-temperature relation, $R_T=a(1+b\overline{T}+c\overline{T}^2)$, respectively. The average temperatures of the test tube between the two electrodes, V_{R4}, were compared with those between first and fourth potential taps, V_R, and much difference for a heat loss could not be clearly observed in high subcooling range. The heat generation rates of the SUS304 test tube between the first and forth potential taps, $Q=I^2R_T$, and between adjacent potential taps (first and second potential taps, $Q_1=I^2R_{T1}$, second and third ones, $Q_2=I^2R_{T2}$, and third and fourth ones, $Q_3=I^2R_{T3}$) were calculated from the measured voltage difference between the first and forth potential taps and between adjacent potential taps of the SUS304 test tube, V_R, V_{R1}, V_{R2} and V_{R3}, and that across the standard resistance, V_I. The surface heat fluxes between the first and forth potential taps and between adjacent potential taps, q, q_1, q_2 and q_3, are the differences between the heat generation rate per unit surface area, Q, Q_1, Q_2 and Q_3, and the rate of change of energy storage in the SUS304 test tube obtained from the faired average temperature versus time curve as follows:

$$q=\frac{V}{S}\left(Q-\rho c\frac{d\overline{T}}{dt}\right) \tag{6}$$

where ρ, c, V and S are the density, the specific heat, the volume and the inner surface area of the SUS304 test tube, respectively.

The heater inner surface temperatures between the first and forth potential taps and between adjacent potential taps, T_s, T_{s1}, T_{s2} and T_{s3}, were also obtained by solving the steady one-dimensional heat conduction equation in the test tube under the conditions of measured

average temperature, $\overline{T}$, and surface heat flux of the test tube, q. The solutions for the inner and outer surface temperatures of the test tube, T_s and T_{so}, are given by the steady one-dimensional heat conduction equation. The basic equation for the test tube is as follows:

$$\frac{d^2T}{dr^2}+\frac{1}{r}\frac{dT}{dr}+\frac{Q}{\lambda}=0 \tag{7}$$

then integration yields and the mean temperature of the test tube is obtained.

$$T(r)=-\frac{Qr^2}{4\lambda}+\frac{Qr_o^2}{2\lambda}lnr+C \tag{8}$$

$$\overline{T}=\frac{1}{\pi\left(r_o^2-r_i^2\right)}\int_{r_i}^{r_o}2\pi rT(r)dr \tag{9}$$

Generating heat in the tube is equal to the heat conduction and the test tube is perfectly insulated.

$$q=-\lambda\left.\frac{dT}{dr}\right|_{r=r_i}=\frac{\left(r_o^2-r_i^2\right)Q}{2r_i} \tag{10}$$

$$\left.\frac{dT}{dr}\right|_{r=r_o}=0 \tag{11}$$

The temperatures of the heater inner and outer surfaces, T_s and T_{so}, and C in Eq. (8) can be described as follows:

$$T_s=T(r_i)=\overline{T}-\frac{qr_i}{4(r_o^2-r_i^2)^2\lambda}\left[4r_o^2\left\{r_o^2\left(lnr_o-\frac{1}{2}\right)-r_i^2\left(lnr_i-\frac{1}{2}\right)\right\}-\left(r_o^4-r_i^4\right)\right]-\frac{qr_i}{2(r_o^2-r_i^2)\lambda}\left(r_i^2-2r_o^2lnr_i\right) \tag{12}$$

$$T_{so}=T(r_o)=\overline{T}-\frac{qr_i}{4(r_o^2-r_i^2)^2\lambda}\left[4r_o^2\left\{r_o^2\left(lnr_o-\frac{1}{2}\right)-r_i^2\left(lnr_i-\frac{1}{2}\right)\right\}-\left(r_o^4-r_i^4\right)\right]-\frac{qr_ir_o^2}{2(r_o^2-r_i^2)\lambda}\left(1-2lnr_o\right) \tag{13}$$

$$C=\overline{T}-\frac{qr_i}{4(r_o^2-r_i^2)^2\lambda}\left[4r_o^2\left\{r_o^2\left(lnr_o-\frac{1}{2}\right)-r_i^2\left(lnr_i-\frac{1}{2}\right)\right\}-\left(r_o^4-r_i^4\right)\right] \tag{14}$$

where $\overline{T}$, q, λ, r_i and r_o are average temperature of the test tube, heat flux, thermal conductivity, test tube inner radius and test tube outer radius, respectively.

In case of the 6-mm inner diameter test sections, before entering the test tube, the test water flows through the tube with the same inner diameter of the SUS304 test tube to form the fully developed velocity profile. The entrance tube lengths, L_e, are given 333 mm (L_e/d=55.5). The values of L_e/d for the test tube of d=6 mm at which the center line velocity reaches 99 % of the maximum value for turbulence flow were obtained ranging from 9.8 to 21.9 ($2.77\times10^4 \le Re_d \le 3.08\times10^5$) by the correlation of Brodkey and Hershey [8] as follows:

$$\frac{L_e}{d} = 0.693\, Re_d^{1/4} \tag{15}$$

The inlet and outlet liquid temperatures, T_{in} and T_{out}, were measured by 1-mm o.d., sheathed, K-type thermocouples (*Nimblox*, sheath material: SUS316, hot junction: ground, response time (63.2 %): 46.5 ms) which are located at the centerline of the tube at the upper and lower stream points of 283 and 63 mm from the tube inlet and outlet points for the 6-mm inner diameter test section. The inlet and outlet pressures, P_{ipt} and P_{opt}, were measured by the strain gauge transducers (Kyowa Electronic Instruments Co., Ltd., PHS-20A, Natural frequency: approximately 30 kHz), which were located near the entrance of conduit at upper and lower stream points of 63 mm from the tube inlet and outlet points for d=6 mm inner diameter test section. The thermocouples and the transducers were installed in the conduits as shown in Fig. 2.

The inlet and outlet pressures, P_{in} and P_{out}, for the 6-mm inner diameter test section were calculated from the pressures measured by inlet and outlet pressure transducers, P_{ipt} and P_{opt}, as follows:

$$P_{in} = P_{ipt} - \left\{ \left(P_{ipt}\right)_{wnh} - \left(P_{opt}\right)_{wnh} \right\} \times \frac{L_{ipt}}{L_{ipt} + L + L_{opt}} \tag{16}$$

$$P_{out} = P_{in} - \left(P_{in} - P_{opt}\right) \times \frac{L}{L + L_{opt}} \tag{17}$$

where L_{ipt}=0.063 m and L_{opt}=0.063 m for the 6-mm inner diameter one. Experimental errors are estimated to be ±1 K in inner tube surface temperature and ±2 % in heat flux. Mass velocity, inlet and outlet subcoolings, inlet and outlet pressures and exponential period were measured within the accuracy ±2 %, ±1 K, ±4 kPa and ±2 %, respectively.

3. NUMERICAL SOLUTION OF TURBULENT HEAT TRANSFER

3.1. RANS Equations for k-ε Turbulence Model with High Reynolds Number Form

The RANS equations for k-ε turbulence model [9] in a circular tube of 3 mm in diameter and 526 mm long were numerically solved for heating of water with heated section of 3 mm in diameter and 67 mm long by using PHOENICS code under the same conditions as the experimental ones and with temperature dependent thermo-physical fluid properties [10]. The unsteady RANS equations for turbulent heat transfer are expressed in the three dimensional coordinate shown in Fig. 5 as follows [11].

(Continuity Equation) Cylindrical coordinates (r, θ, z):

$$\frac{\partial \rho}{\partial t}+\frac{1}{r}\frac{\partial}{\partial r}(ru_r\rho)+\frac{1}{r}\frac{\partial}{\partial \theta}(u_\theta\rho)+\frac{\partial}{\partial z}(u_z\rho)=0 \tag{18}$$

(Momentum Equation) Cylindrical coordinates (r, θ, z)

r-component:

$$\frac{\partial}{\partial t}(\rho u_r)+\frac{\partial}{\partial r}(\rho u_r u_r)+\frac{1}{r}\frac{\partial}{\partial \theta}(\rho u_\theta u_r)-\frac{\rho u_\theta^2}{r}+\frac{\partial}{\partial z}(\rho u_z u_r)=-\frac{\partial P}{\partial r}+\frac{1}{r}\frac{\partial}{\partial r}\left(r\tau_{rr}\right)+\frac{1}{r}\frac{\partial}{\partial \theta}\tau_{r\theta}-\frac{\tau_{\theta\theta}}{r}+\frac{\partial}{\partial z}\tau_{rz}+\rho g_r \tag{19}$$

θ-component:

$$\frac{\partial}{\partial t}(\rho u_\theta)+\frac{\partial}{\partial r}(\rho u_r u_\theta)+\frac{1}{r}\frac{\partial}{\partial \theta}(\rho u_\theta u_\theta)+\frac{\rho u_r u_\theta}{r}+\frac{\partial}{\partial z}(\rho u_z u_\theta)=-\frac{1}{r}\frac{\partial P}{\partial \theta}+\frac{1}{r^2}\frac{\partial}{\partial r}\left(r^2\tau_{r\theta}\right)+\frac{1}{r}\frac{\partial}{\partial \theta}\tau_{\theta\theta}+\frac{\partial}{\partial z}\tau_{\theta z}+\rho g_\theta \tag{20}$$

z-component:

$$\frac{\partial}{\partial t}(\rho u_z)+\frac{\partial}{\partial r}(\rho u_r u_z)+\frac{1}{r}\frac{\partial}{\partial \theta}(\rho u_\theta u_z)+\frac{\partial}{\partial z}(\rho u_z u_z)=-\frac{\partial P}{\partial z}+\frac{1}{r}\frac{\partial}{\partial r}\left(r\tau_{rz}\right)+\frac{1}{r}\frac{\partial}{\partial \theta}\tau_{\theta z}+\frac{\partial}{\partial z}\tau_{zz}+\rho g_z \tag{21}$$

(Energy Equation) Cylindrical coordinates (r, θ, z):

$$\begin{aligned}&\rho\frac{\partial h}{\partial t}+\rho\frac{\partial}{\partial r}(u_r h)+\rho\frac{1}{r}\frac{\partial}{\partial \theta}(u_\theta h)+\rho\frac{\partial}{\partial z}(u_z h)=\\&\frac{1}{r}\frac{\partial}{\partial r}\left\{\left(\lambda+c_p\frac{\mu_t}{\sigma_t}\right)r\frac{\partial T}{\partial r}\right\}+\frac{1}{r^2}\frac{\partial}{\partial \theta}\left\{\left(\lambda+c_p\frac{\mu_t}{\sigma_t}\right)\frac{\partial T}{\partial \theta}\right\}+\frac{\partial}{\partial z}\left\{\left(\lambda+c_p\frac{\mu_t}{\sigma_t}\right)\frac{\partial T}{\partial z}\right\}+Q\end{aligned} \tag{22}$$

(Transport Equation for k) Cylindrical coordinates (r, θ, z):

$$\begin{aligned}&\rho\frac{\partial k}{\partial t}+\rho\frac{\partial}{\partial r}(u_r k)+\rho\frac{1}{r}\frac{\partial}{\partial \theta}(u_\theta k)+\rho\frac{\partial}{\partial z}(u_z k)=\\&\frac{1}{r}\frac{\partial}{\partial r}\left\{\left(\mu+\frac{\mu_t}{\sigma_k}\right)r\frac{\partial k}{\partial r}\right\}+\frac{1}{r^2}\frac{\partial}{\partial \theta}\left\{\left(\mu+\frac{\mu_t}{\sigma_k}\right)\frac{\partial k}{\partial \theta}\right\}+\frac{\partial}{\partial z}\left\{\left(\mu+\frac{\mu_t}{\sigma_k}\right)\frac{\partial k}{\partial z}\right\}+\rho(P_k+\Gamma_b-\varepsilon)\end{aligned} \tag{23}$$

(Transport Equation for ε) Cylindrical coordinates (r, θ, z):

$$\begin{aligned}&\rho\frac{\partial \varepsilon}{\partial t}+\rho\frac{\partial}{\partial r}(u_r \varepsilon)+\rho\frac{1}{r}\frac{\partial}{\partial \theta}(u_\theta \varepsilon)+\rho\frac{\partial}{\partial z}(u_z \varepsilon)=\\&\frac{1}{r}\frac{\partial}{\partial r}\left\{\left(\mu+\frac{\mu_t}{\sigma_\varepsilon}\right)r\frac{\partial \varepsilon}{\partial r}\right\}+\frac{1}{r^2}\frac{\partial}{\partial \theta}\left\{\left(\mu+\frac{\mu_t}{\sigma_\varepsilon}\right)\frac{\partial \varepsilon}{\partial \theta}\right\}+\frac{\partial}{\partial z}\left\{\left(\mu+\frac{\mu_t}{\sigma_\varepsilon}\right)\frac{\partial \varepsilon}{\partial z}\right\}\\&+\rho\frac{\varepsilon}{k}(C_{1e}P_k+C_{3e}\Gamma_b-C_{2e}\varepsilon)\end{aligned} \tag{24}$$

where $\tau_{rr}=2\rho\nu\frac{\partial u_r}{\partial r}$ (25)

$$\tau_{\theta\theta}=2\rho\nu\left(\frac{1}{r}\frac{\partial u_\theta}{\partial \theta}+\frac{u_r}{r}\right) \tag{26}$$

$$\tau_{zz}=2\rho\nu\frac{\partial u_z}{\partial z} \tag{27}$$

$$\tau_{r\theta}=\tau_{\theta r}=\rho\nu\left(r\frac{\partial}{\partial r}\left(\frac{u_\theta}{r}\right)+\frac{1}{r}\frac{\partial u_r}{\partial \theta}\right) \tag{28}$$

$$\tau_{\theta z}=\tau_{z\theta}=\rho\nu\left(\frac{\partial u_\theta}{\partial z}+\frac{1}{r}\frac{\partial u_z}{\partial \theta}\right) \tag{29}$$

$$\tau_{zr}=\tau_{rz}=\rho\nu\left(\frac{\partial u_z}{\partial r}+\frac{\partial u_r}{\partial z}\right) \tag{30}$$

$$g_r=0,\quad g_\theta=0,\quad g_z=-g \tag{31}$$

$$h=c_p T \tag{32}$$

$$\nu_t = C_\mu \frac{k^2}{\varepsilon} \tag{33}$$

$$P_k = \nu_t \left[2\left\{ \left(\frac{\partial u_r}{\partial r}\right)^2 + \left(\frac{1}{r}\frac{\partial u_\theta}{\partial \theta} + \frac{u_r}{r}\right)^2 + \left(\frac{\partial u_z}{\partial z}\right)^2 \right\} + \left(\frac{1}{r}\frac{\partial u_r}{\partial \theta} + \frac{\partial u_\theta}{\partial r} - \frac{u_\theta}{r}\right)^2 + \left(\frac{\partial u_\theta}{\partial z} + \frac{1}{r}\frac{\partial u_z}{\partial \theta}\right)^2 + \left(\frac{\partial u_z}{\partial r} + \frac{\partial u_r}{\partial z}\right)^2 \right] \tag{34}$$

$$\Gamma_b = \frac{-\nu_t}{\rho \sigma_t}\left(g_r \frac{\partial \rho}{\partial r} + g_\theta \frac{1}{r}\frac{\partial \rho}{\partial \theta} + g_z \frac{\partial \rho}{\partial z} \right) \tag{35}$$

$$\lambda_e = \lambda_t + \lambda \tag{36}$$

$$\lambda_t = \frac{c_p \mu_t}{\sigma_t} \tag{37}$$

$$\nu = \frac{\mu}{\rho} + \nu_t \tag{38}$$

u_r, u_θ and u_z are the r, θ and z components of a velocity vector, respectively. The constants, σ_k, σ_ε, σ_t, C_{1e}, C_{2e}, C_{3e} and C_μ, appearing in Eqs. (22) to (24), (33), (35) and (37) take the values given in Table 1.

3.2. Boundary Conditions

The fundamental equations are numerically analyzed together with the following boundary conditions. On the outer boundary of heated section: constant heat flux, and non-slip condition.

$$q = -\lambda \frac{\partial T}{\partial r} = constant \tag{39}$$

At the outer boundary of non-heated section:

$$\frac{\partial T}{\partial r} = 0 \tag{40}$$

At the lower boundary:

$$T = T_{in}, \quad u_r = 0, \quad u_\theta = 0 \quad and \quad u_z = u \qquad \text{for in-flow} \tag{41}$$

where T_{in} and u are a inlet liquid temperature and a flow velocity at the entrance of the test section.

3.3. Method of solution

The control volume discretization equations were derived from these fundamental equations by using the hybrid scheme [12]. The thermo-physical properties for each control volume are given by each control volume temperature numerically analyzed. The procedure for the calculation of the flow field is the SIMPLE algorithm which stands for Semi-Implicit Method for Pressure-Linked Equations [13]. A uniform heat flux, q, was prescribed at the heated pipe wall for the range of 2.73×10^5 to 3.04×10^7 W/m^2 as a boundary condition, and numerical calculation was continued until the steady-state was obtained. The surface temperature on the test tube, T_s, was analyzed from the calculated temperature of the outer control volume on the test tube surface, *TEM*, which is located on the center of the control volume, by solving the heat conduction equation in liquid as follows [14, 15].

$$T_s = \frac{q}{\lambda_l}\frac{(\Delta r)_{out}}{2} + TEM \tag{42}$$

where, $(\Delta r)_{out}$ is the outer control volume width on the r-component. Average heat transfer coefficient on the test tube surface was obtained by $T_{s,av}$ averaging the calculated local surface temperatures, $(T_s)_z$, at every 0.5 mm in the heated length, L. The flow and temperature field predictions were obtained using the PHOENICS CFD code [10].

4. RESULTS AND DISCUSSION

4.1. Experimental Conditions and Parameters used for Calculation

Steady-state heat transfer processes on the SUS304 test tubes of 6 mm inner diameter that caused by the exponentially increasing heat inputs, $Q_0 exp(t/\tau)$, were measured. The exponential periods, τ, of the heat input ranged from 7.02 to 8.5 s. The initial experimental conditions such as inlet flow velocity, inlet liquid temperature, inlet pressure and exponential period for the CHF experiment were determined independent of each other before each experimental run.

The experimental conditions were as follows:

Test Tube Number	THD-F191 and THD-F196
Heater material	SUS304
Surface condition	Commercial finish of inner surface
Surface roughness	3.89 μm for *Ra*, 21.42 μm for *Rmax* and 15.03 μm for *Rz*
Inner diameter (d)	6 mm
Heated length (L)	59.5 and 59.7 mm
Effective Length (L_{eff})	49.0 and 50.2 mm
L_{12}, L_{23} and L_{34}	16.5, 16.8 and 15.7 mm for THD-F191 and 16.8, 17.3 and 16.1 mm for THD-F196
L/d	9.92 and 9.95
L_{eff}/d	8.17 and 8.37
Wall thickness (δ)	0.5 mm
Inlet flow velocity (u)	3.95 to 30.80 m/s
Liquid Reynolds numbers (Re_d)	3.65×10^4 to 3.08×10^5
Inlet pressure (P_{in})	785.01 to 966.89 kPa
Outlet pressure (P_{out})	799.60 to 845.11 kPa
Inlet subcooling ($\Delta T_{sub,in}$)	141.35 to 159.03 K

Outlet subcooling ($\Delta T_{sub,out}$)	109.56 to 134.41 K
Inlet liquid temperature (T_{in})	288.10 to 308.73 K
Exponentially increasing heat input (Q)	$Q_0 exp(t/\tau)$, τ=7.02 to 8.51 s

The parameters used for calculation were as follows:

Inner diameter (d)	3 mm
Heated length (L)	67 mm
Entrance length (L_e)	282 mm
Exit length (L_{ex})	177 mm
Test section length (L_{ts})	526 mm
Heat flux (q)	2.73×10^5 to 3.04×10^7 W/m^2 ($q_0 exp(t/\tau)$, τ=6.24 to 6.60 s)
Inlet flow velocity (u)	4.14, 7.47, 10.40 and 13.83 m/s
Liquid Reynolds numbers (Re_d)	2.77×10^4 to 7.57×10^4
Inlet liquid temperature (T_{in})	300.74 to 303.18 K
Coordinate system	cylindrical coordinate (r, θ, z)
Control volume number	(17 to 45, 60, 896)
Physical model	k-ε turbulence model with high Reynolds number form
Wall functions	logarithmic law ($23.04 \le y^+ \le 25.26$)

4.2. Steady State Heat Transfer Characteristics

4.2.1. SUS304 test tube of 6 mm inner diameter

Figure 6 shows typical examples of the heat transfer curves for the exponential period, τ, of around 8.02 s on the THD-F191 SUS304 test tube of d=6 mm and L_{eff}=49.0 mm with the

rough finished inner surface (Ra=3.89 μm) at the inlet liquid temperature, T_{in}, of 295.83 to 308.73 K and the flow velocities, u, of 3.95 to 30.80 m/s. At the flow velocities of 4.0 and 9.9 m/s (red and green solid lines), the heat flux gradually becomes higher with an increase in inner surface superheat, ΔT_{sat} ($=T_s-T_{sat}$, T_s: heater inner surface temperature and T_{sat}: saturation temperature), on the non-boiling forced convection curve derived from our correlation, Eq. (43), [16] up to the point where the slope begins to increase with heat flux following the onset of nucleate boiling:

$$Nu_d = 0.02\, Re_d^{0.85}\, Pr^{0.4}\left(\frac{L}{d}\right)^{-0.08}\left(\frac{\mu}{\mu_w}\right)^{0.14} \tag{43}$$

All properties in the equation are evaluated at the average bulk liquid temperature, T_L, [$=(T_{in}+(T_{out})_{cal})/2$], except μ_w, which is evaluated at the heater inner surface temperature. After that the heat flux increases along the fully developed nucleate boiling curve on the graph up to the CHF, at which the transition to film boiling occurs with the rapidly increasing of surface superheat. It is assumed that the transition to film boiling would occur due to the hydro-dynamic instability suggested by Kutateladze [6] and Zuber [7]. At flow velocities of 21 and 30 m/s (blue and black solid lines), the heat flux gradually becomes higher with an increase in ΔT_{sat} on the non-boiling forced convection curve derived from our correlation, Eq. (43), up to the CHF, at which the transition to film boiling occurs on the non-boiling forced convection curve. Although the violent boiling takes place for a period of time before the CHF point, the slope on the boiling curve does not increase with heat flux even following the onset of nucleate boiling. It is assumed that the transition to film boiling would occur due to the heterogeneous spontaneous nucleation at the lower limit of the heterogeneous spontaneous nucleation temperature at the steady-state CHF but not due to the hydro-dynamic instability. However the CHFs do not extremely become lower than the values calculated from our CHF correlations. The CHF and its surface superheat become higher with an increase in flow

velocity. The fully developed nucleate boiling curves for the flow velocity lower than 9.9 m/s and the heat transfer curves in higher heat flux range for the flow velocity higher than 21 m/s agree with each other forming a single straight line calculated from Eq. (44) on the *log q* versus *log* ΔT_{sat} graph.

$$q = C\Delta T_{sat}^{n} = 1.065\times10^{5}\Delta T_{sat}^{1.2} \tag{44}$$

where *C* and *n* are coefficient and exponent, and equivalent to 1.065×10^5 and 1.2 respectively. The correlation closely describes the fully developed nucleate boiling curves for the flow velocity lower than 9.9 m/s and the nucleate boiling curves in higher heat flux range for the flow velocity higher than 21 m/s on the SUS304 test tube of d=6 mm and L_{eff}=49.0 mm with the rough finished inner surface at the outlet pressure of around 800 kPa obtained in this work within ±30 % differences under the wide range of flow velocities.

The equation of incipient boiling superheat given by Bergles and Rohsenow [17] is also shown in the figure for comparison.

$$(\Delta T_{sat})_{ONB} = 0.556\left(\frac{q}{1082P^{1.156}}\right)^{0.463P^{0.0234}} \tag{45}$$

where q is the surface heat flux in W/m^2, P is the system pressure in bar and ΔT_{sat} is in K. The corresponding curves derived from the correlations for fully developed subcooled boiling given by Rohsenow [18] are also shown in Fig. 6 for comparison.

$$\frac{c_{pl}\Delta T_{sat}}{h_{fg}} = C_{sf}\left(\frac{q}{\mu_l h_{fg}}\sqrt{\frac{\sigma}{g(\rho_l-\rho_g)}}\right)^{0.33}\left(\frac{c_{pl}\mu_l}{\lambda_l}\right)^{1.7} \tag{46}$$

where the various fluid properties are evaluated at the saturation temperature corresponding to the local pressure and C_{sf} is a function of the particular heating surface-fluid combination. The value of n given by Rohsenow correlation, Eq. (46), with C_{sf}=0.03 is about 2.5 times larger than that of our correlation, Eq. (44), on the *log q* versus *log* ΔT_{sat} graph. The values of the

lower limit of the heterogeneous spontaneous nucleation temperature, T_{HET}, [5] and the homogeneous spontaneous nucleation temperature, T_H, [19] at the pressure of 800 kPa are shown in the figure for comparison. The inner surface temperature of the test tube at CHF with the flow velocity, u, of 30 m/s is almost 143.13 and 88.41 K higher than the lower limit of the heterogeneous spontaneous nucleation temperature and the homogeneous spontaneous nucleation temperature, respectively.

Figure 6 also shows the relation between the heat flux, q, and the outer surface temperature of the test tube in the open air, T_{so}, on the *log* q versus *log* $\Delta T_{so,sat}$ ($=T_{so}-T_{sat}$) graph for the SUS304 test tube of d=6 mm and L_{eff}=49.0 mm with the rough finished inner surface (Ra=3.89 μm) with the exponential period of 8.02 s at the flow velocities of 4.0, 9.9, 21 and 30 m/s (red, green, blue and black one dot broken lines). The values of T_{so} are derived from our correlation, Eq. (13). And the outer surface temperature of the test tube, T_{so}, was continuously measured in the time interval of 3 seconds by an infrared thermal imaging camera (ITIC). These experimental data are shown as solid circles with each symbol color in the figure. These outer surface temperatures were almost 8 % lower than the values calculated from Eq. (13) for each heat flux in the whole velocity, although the infrared thermal imaging camera has the accuracy of ±2 % of reading.

Typical example of the heat transfer curves and the relation between the heat flux, q, and the outer surface temperature of the test tube in the open air, T_{so}, on the THD-F196 SUS304 test tube of d=6 mm and L_{eff}=50.2 mm with the rough finished inner surface (Ra=3.89 μm) are also shown on the *log* q versus *log* ΔT_{sat} ($=T_s-T_{sat}$) graph and the *log* q versus *log* $\Delta T_{so,sat}$ ($=T_{so}-T_{sat}$) one for the exponential period, τ, of around 8.10 s at the inlet liquid temperature, T_{in}, of 288.10 to 298.96 K and the flow velocities, u, of 4.05 to 30.56 m/s in Fig. 7. The color

temperatures of outer surface of the test tube in the open air have been observed by a video camera (VC) and the photographs at each CHF point are shown beside the figure for each flow velocity. The color temperature of outer surface of the test tube at the flow velocity of 30 m/s would reach up to around 1173 K because the test tube begins to be shining white. It is assumed from these facts that the CHFs on the SUS304 test tube would explicitly occur due to the **heterogeneous spontaneous nucleation** with combinations of non-boiling forced convection heat transfer and heterogeneous spontaneous nucleation temperature in independence of surface conditions such as surface roughness and surface wettability for the flow velocity higher than 21 m/s. Cavities of submicron sizes from which bubble nucleation can occur at high surface superheat and heat flux would exist but not sufficient in their numbers to flatten the temperature gradient near the heated surface through the bubble motion and the latent heat transport. Therefore, the nucleate boiling heat transfer for higher flow velocity would be like the non-boiling forced convection one.

The effect of flow velocity on the values of ΔT_{sat} (=T_s-T_{sat}) and $\Delta T_{so,sat}$ (=T_{so}-T_{sat}) at the CHF points, $(\Delta T_{sat})_{cr}$ and $(\Delta T_{so,sat})_{cr}$, for the VERTICAL SUS304 tubes of d=3 and 6 mm were represented as a function of the flow velocity, u, in Fig. 8. The values of $(\Delta T_{sat})_{cr}$, (●, ● and ●), for VERTICAL SUS304 test tube of d=6 mm in this work become linearly higher with an increase in the flow velocity for the flow velocities ranging from 3.95 to 30.80 m/s, although those, (▲ and ●), for the VERTICAL SUS304 test tubes of d=3 and 6 mm [1, 2] are almost constant [$(\Delta T_{sat})_{cr}$=100 K] for the u higher than 9.9 m/s. Under the VERTICAL test tubes in this work, the values of $(\Delta T_{sat})_{cr}$, (●, ● and ●), becomes lower than those, (▲ and ●), at the flow velocity of 3.95 m/s and those becomes higher at the flow velocities higher than 6.9 m/s. These SUS304 test tubes were not the same serial number but the same manufacturer. It is contemplated especially in case of VERTICAL SUS304 test tubes, (●, ● and ●), that the

heterogeneous spontaneous nucleation temperature would become higher due to a difference between surface conditions of test tubes. The discrepancy between surface conditions such as surface roughness and surface wettability would play an important role in nucleate boiling heat transfer at the CHF points. The values of $(\Delta T_{so,sat})_{cr}$, (○, ○ and ○), for VERTICAL SUS304 test tube of d=6 mm in this work become linearly higher with an increase in the flow velocity for the flow velocities ranging from 3.95 to 30.80 m/s. These values of ΔT_{sat} and $(\Delta T_{so,sat})_{cr}$, for THD-F196 SUS304 test tube (● and ○) become T_s=494.27 and T_{so}=712.44 K at u=4 m/s, T_s=563.08 and T_{so}=885.09 K at u=9.9 m/s, T_s=591.97 and T_{so}=980.38 K at u=21 m/s and T_s=667.20 and T_{so}=1170.93 K at u=30 m/s.

4.2.2. Platinum test tube of 3 mm inner diameter [4]

Figure 9 has been shown typical examples of the heat transfer curves for the exponential period, τ, of around 8 s on the Platinum test tube of d=3 mm and L=66.5 mm at the inlet liquid temperature, T_{in}, of around 301.73 K and the flow velocities, u, of 4 to 13.3 m/s [4]. At a fixed flow velocity, the heat flux gradually becomes higher with an increase in $\Delta \overline{T}_{sat}$ ($=\overline{T}_s - T_{sat}$) on the non-boiling forced convection curve derived from our correlation, Eq. (43), [16] up to the point where the slope begins to increase with heat flux following the onset of nucleate boiling. And the heat flux increases up to the CHF where the heater surface temperature rapidly jumps from the nucleate boiling heat transfer regime to the film boiling one. The CHF and its superheat become higher with an increase in flow velocity. The nucleate boiling curves in higher heat flux range for each flow velocity agree with each other forming a single straight line on the *log q* versus *log* $\Delta \overline{T}_{sat}$ graph. The analytical solution of incipient boiling superheat given by Sato and Matsumura [20] is shown in the figure for comparison. The solution was derived based on the initiation model of bubble growth.

$$q = \frac{\lambda_l h_{fg} \left(T_s - T_{sat}\right)^2}{8\sigma T_{sat} \left(v_g - v_l\right)} \tag{47}$$

The thermo-physical properties are defined at the saturated temperature, T_{sat}. The experimental data of the incipient boiling superheat for each flow velocity almost agree with the values predicted by Eq. (47). The equation of incipient boiling superheat given by Bergles and Rohsenow [17] is also shown in the figure for comparison. The values of $(\Delta T_{sat})_{ONB}$ calculated from Eq. (45) are in good agreement with the experimental data of the incipient boiling superheat for each flow velocity. The fully developed subcooled boiling curve for Platinum test tube with a commercial finish of inner surface can be expressed by the following empirical correlation [4].

$$q = C\Delta\overline{T}_{sat}^{\,n} = 463\Delta\overline{T}_{sat}^{\,3} \tag{48}$$

where C and n are coefficient and exponent, and equivalent to 463 and 3 respectively. The correlation can almost describe the fully developed subcooled boiling curves for the Platinum test tube of d=3 mm and L=66.5 mm with the commercial finish of inner surface at the outlet pressure of around 800 kPa obtained in this work within 15 % difference under the wide range of flow velocities. The corresponding curves derived from the correlations, Eq. (46) with C_{sf}=0.014, Eqs. (49) to (52), for fully developed subcooled boiling given by Rohsenow [18], McAdams et al. [21], Jens and Lottes [22] and Thom et al. [23] are also shown in Fig. 9 for comparison.

- McAdams et al. [21]:

$\Delta T_{sat} = 22.62 q^{0.259}$ for dissolved gas concentration of 0.3 ml of air per liter of water (49)

$\Delta T_{sat} = 28.92 q^{0.259}$ for dissolved gas concentration of 0.06 ml of air per liter of water (50)

where ΔT_{sat} is in K and q is in MW/m^2.

- Jens and Lottes [22]:

$$\Delta T_{sat} = 0.79 q^{0.25} e^{-P/6.2} \tag{51}$$

where P is the absolute pressure in MPa, ΔT_{sat} is in K and q is in W/m^2.

- Thom et al. [23]:

$$\Delta T_{sat} = 0.022 q^{0.5} e^{-P/8.6} \tag{52}$$

where P is the absolute pressure in MPa, ΔT_{sat} is in K and q is in W/m^2. The values of n given by McAdams et al. correlation and Jens and Lottes one are about 30 % larger than that of our correlation, although that of Thom et al. correlation is about 30 % smaller. The values calculated from our correlation are in good agreement with the corresponding values for Rohsenow correlation, Eq. (46), with C_{sf}=0.014 on the *log q* versus *log* $\Delta \overline{T}_{sat}$ graph. The values of the lower limit of the heterogeneous spontaneous nucleation temperature, T_{HET}, [5] and the homogeneous spontaneous nucleation temperature, T_H, [19] at the pressure of 800 kPa are shown in the figure for comparison. The inner surface temperature of the test tube at CHF with the flow velocity, u, of 13.3 m/s is 41.31 and 96.03 K lower than the T_{HET} and the T_H, respectively.

4.2.2.1. Thickness of conductive sub-layer, δ_{CSL}, for nucleate boiling heat transfer

The numerical solutions of the theoretical equations for k-ε turbulence model with high Reynolds number form are in good agreement with the experimental data and the values derived from Eq. (43) within -15 % difference as shown in Fig 9. In Fig. 10, the test tube surface is located at r=-1.5 mm and the conductive sub-layer [14, 15] exists on the test tube surface. The liquid temperatures in the conductive sub-layer on the test tube surface will become linearly lower with a decrease in the radius by the heat conduction from the surface temperature on the test tube, $T_f=T_s-\Delta rq/\lambda_l$. And let those, T_f, equal the calculated liquid temperature of the outer control volume on the test tube surface, *TEM*, in the turbulent flow region, which is located on the center of the control volume as given in Eq. (42). Half the

outer control volume width for the *r*-component, $(\Delta r)_{out}/2$, would become the thickness of the conductive sub-layer, δ_{CSL}, for the turbulent heat transfer in a circular tube under two-phase model classified into conductive sub-layer and inner region of the turbulent flow [24]. The thicknesses of the conductive sub-layer, δ_{CSL}, for the turbulent heat transfer on the Pt test tube of d=3 mm and L=66.5 mm in Fig 9 are 18.1, 10.35, 8.01 and 6.52 μm at flow velocities, u, of 4.0, 6.9, 9.9 and 13.3 m/s, respectively. The numerical solutions of the theoretical equations for k-ε turbulence model with low Reynolds number form are shown in APPENDIX A.3. Those are scattered and do not also fit in with the experimental data. The δ_{CSL} would not be precisely established from those steady-state turbulent heat transfer curves.

The heat transfer with thinner conductive sub-layer dissipated by the evaporation on nucleate boiling is numerically analyzed by the theoretical equations for steady-state turbulent heat transfer. The numerical solutions for the relation between the heat flux, q, and the temperature difference between average inner surface temperature and liquid bulk mean temperature, ΔT_L, are shown for the heat flux, q, ranging from 5.22×10^5 to 1.29×10^7 W/m^2, from 5.45×10^5 to 2.26×10^7 W/m^2, from 5.44×10^5 to 2.59×10^7 W/m^2 and from 5.42×10^5 to 3.04×10^7 W/m^2 at the flow velocities of 4.14, 7.47, 10.40 and 13.83 m/s as colored open circles in Figs. 11 to 14, respectively. The 11, 12-13, 14 and 12-14 different values for the numerical solutions are plotted for the ΔT_L ranging from 4.39 to 291.75 K, from 3.02 to 265.38 K, from 2.77 to 314.95 K and from 3.05 to 236.70 K on the $log\ q$ versus $log\ \Delta T_L$ graph, respectively. These solutions for δ=7.28, 3.49, 0.78 and 0.1 μm, δ=5.04, 1.34, 0.51 and 0.09 μm, δ=4.07, 1.52 and 0.43 μm and δ=3.48, 1.37 and 0.41 μm become also higher with an increase in the ΔT_L on the higher curves parallel to the steady-state turbulent heat transfer one derived from Eq. (43) as shown in Figs. 11 to 14, respectively. The outer control volume widths for the *r*-component, $(\Delta r)_{out}$, which are twice as large as the thicknesses of the conductive sub-layer, δ, are ranging from

14.56 to 0.2 μm, ranging from 10.08 to 0.18 μm, ranging from 8.14 to 0.86 μm and ranging from 6.96 to 0.82 μm at flow velocities, u, of 4.14, 7.47, 10.40 and 13.83 m/s, respectively. These curve-fitted numerical solutions based on the least squares method of power-law are shown in Figs. 11 to 14. The thicknesses of the conductive sub-layer, δ, on the nucleate boiling heat transfer experimentally obtained would become half the outer control volume width for the r-component, $(\Delta r)_{out}/2$, numerically solved at an intersection point between the nucleate boiling heat transfer curves and the smoothing curves of conductive sub-layer.

We have assumed that the measurement of thickness of the conductive sub-layer at CHF point would be very useful to discuss the mechanism of the critical heat flux during flow boiling of subcooled water, which would occur due to the heterogeneous spontaneous nucleation at the lower limit of the heterogeneous spontaneous nucleation temperature [5], due to the hydro-dynamic instability suggested by Kutateladze [6] and Zuber [7] or due to the liquid sub-layer dry-out models suggested by Lee and Mudawar [25], Katto [26] and Celata et. al. [27]. The thicknesses of the conductive sub-layer on forced convection and nucleate boiling heat transfer, δ_{CSL} and δ, are shown versus heat flux, q, for the u ranging from 4 to 13.3 m/s in Fig. 15. These thicknesses on the semi-log graph (δ_{CSL}, δ versus $log\ q$) become linearly lower with an increase in the q. Those look like being almost 0 μm at the CHF points, although that at u=4 m/s becomes almost 0 μm at the heat flux 29.32 % lower than the CHF one. The conductive sub-layer at CHF point would have almost disappeared, although the violent boiling noise was made for a period of time before the CHF point. As shown in Fig. 16, the ratios of conductive sub-layer on nucleate boiling heat transfer to conductive sub-layer on forced convection, $\delta_{CSL}/\delta_{CSL}$ and δ/δ_{CSL}, for the Pt test tube of d=3 mm with the commercial finished inner surface can be expressed for the ratios of boiling number on nucleate boiling heat transfer to boiling number at CHF point, Bo/Bo_{cr}, for the u ranging from 4 to 13.3 m/s by

the following correlations:

$$\frac{\delta}{\delta_{CSL}} = -0.7923\, ln\left(\frac{1}{0.6798}\frac{Bo}{Bo_{cr}}\right) \qquad \text{for } u\text{=4 m/s} \qquad (53)$$

$$\frac{\delta}{\delta_{CSL}} = -0.9077\, ln\left(\frac{Bo}{Bo_{cr}}\right) \qquad \text{for } u\text{=6.9 to 13.3 m/s} \qquad (54)$$

It is assumed that the transition to film boiling at the subcooled water flow boiling on the Pt test tube of d=3 mm and L=66.5 mm would occur due to the **liquid sub-layer dry-out model** at the steady-state CHF but not due to the heterogeneous spontaneous nucleation and the hydro-dynamic instability. The conductive sub-layer at CHF point has almost disappeared under the u ranging from 4 to 13.3 m/s, and it would not be seen that the CHF phenomenon occurs at some critical velocity in the vapor phase when the vapor jets and the liquid ones start interfering with each other. It is the reason not to occur the hydrodynamic instability on the vapor-liquid interface at the CHF.

The values of CHF numerically analyzed from Celata et. al.'s liquid sub-layer dry-out model [27] are shown in Figs. 11 to 15 for comparison. The values derived from liquid sub-layer dry-out model are in good agreement with the experimental values of CHF for the Pt test tube of d=3 mm and L=66.5 mm within -9.67 to 11.90 % differences at whole u range of 4.14, 7.47, 10.40 and 13.83 m/s tested here.

5. SUMMARY OF RESULTS

The subcooled boiling heat transfer and the steady state critical heat flux (CHF) in a vertical circular tube for the liquid Reynolds numbers (Re_d=2.77×10^4 to 3.08×10^5), the flow velocities (u=3.95 to 30.80 m/s), the inlet liquid temperatures (T_{in}=288.10 to 308.73 K), the inlet pressures (P_{in}=785.01 to 966.89 kPa) and the exponentially increasing heat input

($Q=Q_0 exp(t/\tau)$, τ=7.02 to 8.51 s) are systematically measured. The SUS304 test tube of inner diameter (d=6 mm), heated lengths (L=59.5 and 59.7 mm), effective length (L_{eff}=49.0 and 50.2 mm), L/d (=9.92 and 9.95), L_{eff}/d (=8.17 and 8.37), and wall thickness (δ=0.5 mm) with average surface roughness (Ra=3.89 μm) is used. The outer surface temperature of the SUS304 test tube with heating is observed by an infrared thermal imaging camera and a video camera. On the other hand, the RANS equations with k-ε turbulence model in a circular tube of a 3 mm in diameter and a 526 mm long are numerically solved for heating of water on heated section of a 3 mm in diameter and a 67 mm long with various thicknesses of conductive sub-layer by using PHOENICS code under the same conditions as the experimental ones previously obtained and with temperature dependent thermo-physical fluid properties. Experimental and computational study results lead as follows:

1) The fully developed nucleate boiling curves for the flow velocity lower than 9.9 m/s and the heat transfer curves in higher heat flux range for the flow velocity higher than 21 m/s agree with each other forming a single straight line calculated from Eq. (44) on the *log q* versus *log* ΔT_{sat} graph.

$$q = C\Delta T_{sat}^{n} = 1.065\times10^{5}\Delta T_{sat}^{1.2} \tag{44}$$

2) The CHFs on the SUS304 test tube would explicitly occur due to the **heterogeneous spontaneous nucleation** with combinations of non-boiling forced convection heat transfer and heterogeneous spontaneous nucleation temperature in independence of surface conditions such as surface roughness and surface wettability for the flow velocity higher than 21 m/s.

3) The thicknesses of the conductive sub-layer, δ_{CSL}, for the turbulent heat transfer on the Pt test tube of d=3 mm and L=66.5 mm are 18.1, 10.35, 8.01 and 6.52 μm at flow velocities, u, of 4.0, 6.9, 9.9 and 13.3 m/s, respectively.

4) The ratios of conductive sub-layer on nucleate boiling heat transfer to conductive sub-layer on forced convection, δ/δ_{CSL}, for the Pt test tube of d=3 mm with the commercial finished inner surface can be expressed for the ratios of boiling number on nucleate boiling heat transfer to boiling number at CHF point, Bo/Bo_{cr}, for the u ranging from 4 to 13.3 m/s by the following correlations:

$$\frac{\delta}{\delta_{CSL}} = -0.7923\, ln\left(\frac{1}{0.6798}\frac{Bo}{Bo_{cr}}\right) \qquad \text{for } u\text{=4 m/s} \qquad (53)$$

$$\frac{\delta}{\delta_{CSL}} = -0.9077\, ln\left(\frac{Bo}{Bo_{cr}}\right) \qquad \text{for } u\text{=6.9 to 13.3 m/s} \qquad (54)$$

5) The transition to film boiling at the subcooled water flow boiling on the Pt test tube of d=3 mm and L=66.5 mm would occur due to the **liquid sub-layer dry-out model** at the steady-state CHF but not due to the heterogeneous spontaneous nucleation and the hydro-dynamic instability.

NOMENCLATURE

Bo $=q/Gh_{fg}$, boiling number

Bo_{cr} $=q_{cr,sub,st}/Gh_{fg}$, boiling number at CHF point

d test tube inner diameter, m

f_F Fanning friction factor

G $=\rho_l u$, mass velocity, kg/m^{2}s

h_{fg} latent heat of vaporization, J/kg

L heated length, m

L_{eff} effective length, m

Nu_d $=hd/\lambda_l$, nusselt number

P_{in} pressure at inlet of heated section, kPa

P_{ipt} pressure measured by inlet pressure transducer, kPa

P_{out} pressure at outlet of heated section, kPa

P_{opt} pressure measured by outlet pressure transducer, kPa

Pr $=c_p\mu/\lambda$, Prandtl number

Q heat input per unit volume, W/m^3

Q_0 initial exponential heat input, W/m^3

q heat flux, W/m^2

$q_{cr,sub,st}$ steady-state CHF for subcooled condition, W/m^2

Ra average roughness, μm

Re_d $=Gd/\mu_l$, Reynolds number

$Rmax$ maximum roughness depth, μm

Rz mean roughness depth, μm

r_i test tube inner radius, m

r_o test tube outer radius, m

$(\Delta r)_{out}$ outer control volume width for r-component, m

TEM calculated temperature of the outer control volume, K

$\bar{T}$ average temperature of test tube, K

$T_{f,av}$ average liquid temperature, K

T_{in} inlet liquid temperature, K

T_L $=(T_{in}+T_{out})/2$, liquid bulk mean temperature, K

T_{out} outlet liquid temperature, K

$(T_{out})_{cal}$ calculated outlet liquid temperature, K

T_s heater inner surface temperature, K

T_{sat} saturation temperature, K

T_{so} heater outer surface temperatures, K

$T_{s,av}$ average inner surface temperature, K

ΔT_L $=(T_{s,av}-T_L)$, temperature difference between average inner surface temperature and liquid bulk mean temperature, K

ΔT_{sat} $=T_s-T_{sat}$, inner surface superheat, K

$\Delta T_{sat,so}$ $=T_s-T_{sat}$, outer surface superheat, K

u flow velocity, m/s

y^+ $=y(\tau_w\rho_l)^{0.5}/\nu_l$, dimensionless normal-distance coordinate

y^+_{CSL} $=(f_F/2)^{0.5}\rho_l u\delta_{CSL}/\mu_l$, non-dimensional thickness of conductive sub-layer

δ conductive sub-layer on nucleate boiling heat transfer

δ_{CSL} $=(\Delta r)_{out}/2$, thickness of conductive sub-layer and conductive sub-layer on forced convection

ε emissivity and rate of dissipation of turbulent energy, m^2/s^3

μ_l viscosity, Ns/m^2

μ_w viscosity at tube wall temperature, Ns/m^2

ν_l $=\mu_l/\rho_l$, kinematic viscosity of fluid, Ns m/kg

ρ_l density of fluid, kg/m^3

τ_w shear stress at the wall, N/m^2

ACKNOWLEDGMENTS

This research was performed as a LHD joint research project of NIFS (National Institute for Fusion Science), Japan, NIFS13KEMF054, 2013 and 2014.

REFERENCES

1. Hata, K., and Masuzaki, S., 2009, “Subcooled Boiling Heat Transfer in a Short Vertical SUS304-Tube at Liquid Reynolds Number Range 5.19×10^4 to 7.43×10^5,” *Nuclear Engineering and Design*, **239**, pp. 2885-2907.

2. Hata, K., and Masuzaki, S., 2010, "Critical Heat Fluxes of Subcooled Water Flow Boiling in a Short Vertical Tube at High Liquid Reynolds Number," *Nuclear Engineering and Design*, **240**, pp. 3145-3157.

3. Hata, K., Shiotsu, M., and Noda, N., 2006, "Critical Heat Flux of Subcooled Water Flow Boiling for High *L/d* Region," *Nuclear Science and Engineering*, **154**, No. 1, pp. 94-109.

4. Hata, K., and Masuzaki, S., 2010, “Subcooled Boiling Heat Transfer for Turbulent Flow of Water in a Short Vertical Tube,” *Journal of Heat Transfer*, Trans. ASME, Series C, **132**, pp. 011501-1-11.

5. Cole, C., 1979, "Homogeneous and heterogeneous nucleation in Boiling Phenomena," Vol. 1, Stralen, S. van, and Cole, R. eds., Hemisphere Pub. Corp., New York, p. 71.

6. Kutateladze, S.S., 1959, “Heat Transfer in Condensation and Boiling,” AEC-tr-3770, USAEC.

7. Zuber, N., 1959, “Hydrodynamic Aspects of Boiling Heat Transfer,” AECU-4439, USAEC.

8. Brodkey, R. S., and Hershey, H. C., 1988, *Transport Phenomena*, McGraw-Hill, New York, p. 568.

9. Jones, W.P., and Launder, B.E., “The Prediction of Laminarization with a Two- equation Model of Turbulence,” *Int. J. Heat Mass Transfer*, **15**, pp.301–314 (1972).

10. Spalding, D.B., 1991, *The PHOENICS Beginner's Guide*, CHAM Ltd., London, United Kingdom.

11. PHOENICS Nihongo Manyuaru (PHOENICS Japanese Manual), 2010, CHAM-Japan, Tokyo (in Japanese).

12. Patankar S.V., 1980, *Numerical Heat Transfer and Fluid Flow*, Hemisphere Pub. Corp., New York.

13. Patankar S.V., and Spalding, D.B., 1972, “A Calculation Procedure for Heat, Mass and Momentum Transfer in Three-Dimensional Parabolic Flows,” *Int. J. Heat Mass Transfer*, **15**, pp.1787–1806.

14. Hata, K., Shirai, Y., Masuzaki, S., and Hamura, A., 2012 “Computational Study of Turbulent Heat Transfer for Heating of Water in a Short Vertical Tube under Velocities Controlled,” *Nuclear Engineering and Design*, **249**, pp. 304-317.

15. Hata, K., Shirai, Y., Masuzaki, S., and Hamura, A., 2012, “Computational Study of Turbulent Heat Transfer for Heating of Water in a Vertical Circular Tube –Influence of Tube Inner Diameter on Thickness of Conductive Sub-layer–,” *Journal of Power and Energy Systems*, **6**, No. 3, pp. 446-461.

16. Hata, K., and Noda, N., 2008, “Turbulent Heat Transfer for Heating of Water in a Short Vertical Tube,” *Journal of Power and Energy Systems*, **2**, No. 1, pp. 318-329.

17. Bergles, A. E., and Rohsenow, W.M., 1964, "The Determination of Forced-Convection Surface-Boiling Heat Transfer," *Journal of Heat Transfer*, Trans. ASME, Series C, **86**, pp. 365-372.

18. Rohsenow, W. M., 1952, "A Method of Correlating Heat-Transfer Data for Surface Boiling of Liquids," Transactions of ASME, **74**, pp. 969-976.

19. Lienhard, J. H., 1976, "Correlation of Limiting Liquid Superheat," *Chem. Eng. Science*, **31**, pp. 847-849.

20. Sato, T., and Matsumura, H., 1963, "On the Conditions of Incipient Subcooled-Boiling with Forced Convection," Bulletin of JSME, Vol. **7**, pp. 392-398.

21. McAdams, W. H., Kennel, W. E., Minden, C. S. L., Carl, R., Picornell, P. M., and Dew, J. E., 1949, "Heat Transfer at High Rates to Water with Surface Boiling," Ind. Engng.

Chem., 41, No.9, pp. 1945-1953.

22. Jens, W. H., and Lottes, P. A., 1951, "Analysis of Heat Transfer Burnout, Pressure Drop and Density Data for High Pressure Water," ANL-4627, May.
23. Thom, J. R. S., Walker, W. M., Fallon, T. A., and Reising, G. F. S., 1966, "Boiling in Subcooled Water during Flow up Heated Tubes or Annuli, Proc. Inst. Mech. Engrs," 180, Pt 3C, pp. 226-246.
24. Hata, K., Fukuda, K., Masuzaki, S., and Hamura, A., 2014, “Conductive Sub-layer of Turbulent Heat Transfer for Heating of Water in a Circular Tube,” Proceedings of the 25th International Symposium on Transport Phenomena, November 5-7, 2014, Krabi Thailand, ISTP-25 Paper 6, pp. 1-10.
25. Lee, C.H., and Mudawar, I., 1988, “A mechanistic critical heat flux model for subcooled flow boiling based on local bulk flow conditions,” *International Journal of Multiphase Flow*, Vol. 14, pp. 711-728.
26. Katto, Y., 1990, "A physical approach to critical heat flux of subcooled flow boiling in round tubes," *International Journal of Heat and Mass Transfer*, Vol. 33, No. 4, pp. 611-620.
27. Celata, G. P., Cumo, M., Mariani, A., Simoncini, M., and Zummo, G., 1994, "Rationalization of existing mechanistic models for the prediction of water subcooled flow boiling critical heat flux," *International Journal of Heat and Mass Transfer* , Vol. 37, suppl. 1, pp. 347-360.

APPENDIX A

A.1. Influence of *L/d* [3]

Figure 17 shows the influence of the *L/d* on the CHF for the inner diameter of 2 mm at fixed inlet subcoolings of 70, 90, 110 and 145 K, respectively. The $q_{cr,sub}$ for the *L/d* ranging from 10.75 to 74.85 were shown versus *L/d* with the flow velocity as a parameter. As shown in these figures, the values of q_{cr} for fixed values of inlet subcooling and flow velocity become exponentially lower with the increase in *L/d* for $L/d \leq 40$ and the decreasing rate becomes lower for $L/d > 40$. The increase in *L/d* indicates the increase of the outlet liquid temperature. The interval of *L/d*, *p*, on which $q_{cr,sub}$ decreases by 1/*e*-fold one and q_0 at *L/d* of 0 for each flow velocity are shown versus Re_d in Fig. 18 and 19, respectively. These experimental data of *p*, q_0 and $q_{cr,sub}$ can be expressed for the *u* ranging from 6.9 to 13.3 m/s by the following correlations:

$$p = C_2 \, Re_d^{\,0.4} \tag{55}$$

$$q_{cr,sub} = q_0 e^{-\frac{(L/d)}{C_2 \, Re_d^{0.4}}} = 0.31414 \times 10^6 \, Re_d^{\,0.4} \, e^{-\frac{(L/d)}{C_2 \, Re_d^{0.4}}} \qquad \text{for } L/d < 40 \tag{56}$$

$$q_{cr,sub} = q_0 e^{-\frac{(L/d)}{C_2 \, Re_d^{0.4}}} = 0.22864 \times 10^6 \, Re_d^{\,0.4} \, e^{-\frac{(L/d)}{C_2 \, Re_d^{0.4}}} \qquad \text{for } L/d > 40 \tag{57}$$

And the energy balance equation for the test tube is given as follows:

$$T_{out} = T_{in} + \frac{4Lq_{cr,sub}}{uc_{pl}\rho_l d} = T_{in} + Sc^* \frac{h_{fg}}{c_{pl}} [1 - e^{-\frac{(L/d)}{C_2 C_3 \, Re_d^{0.4}}}] \tag{58}$$

Thermo-physical properties are evaluated at the liquid bulk mean temperature, $\{T_{in}+(T_{out})_{cal}\}/2$.

A.2. Method of Calculation of Preset Temperature by High-Speed Analog Computer

The subcooled flow boiling heat transfer (HT) and transient critical heat flux (CHF) for the wide ranges of the flow velocity, the inlet subcooling, the outlet pressure and the exponentially increasing heat input are systematically measured. And the authors have given the steady state CHF correlations against inlet and outlet subcoolings based on the effects of

test tube inner diameter (d), flow velocity (u), inlet and outlet subcoolings ($\Delta T_{sub,in}$ and $\Delta T_{sub,out}$) and ratio of heated length to inner diameter (L/d) on CHF. The relation between the steady state CHF, $q_{cr,sub,st}$, and the average temperature of the test tube at CHF, $\overline{T}_{cr}$, for a given experimental condition could be roughly estimated by using boiling curve database and CHF correlation. The power trip temperature (preset temperature), $\overline{T}_{TRIP}$, is given to the heat input control block (a high-speed analog computer) in Fig. 4 as follows:

$$\overline{T}_{TRIP} = \overline{T}_{cr} + \Delta T \tag{59}$$

where, ΔT is increased step by step from 0 to some hundred Kelvins until the measured test tube surface temperature rapidly jumps from the nucleate boiling heat transfer regime to the film boiling one. The maximum value of the heat flux, q, which is larger than the $q_{cr,sub,st}$ is given and that of the heat input per unit volume, Q_v, for the test tube is calculated as follows:

$$q = q_{cr,sub,st} + \Delta q \tag{60}$$

$$Q_v = q\frac{\pi dL}{\pi\{(d+2\delta)^2 - d^2\}L/4} \tag{61}$$

The electrical resistance of the test tube, R_T, is measured at various temperatures before each experiment and the relationship between the electrical resistance and temperature is calibrated by following approximate form.

$$R_T = a(1 + b\overline{T} + c\overline{T}^2) \tag{62}$$

where a, b and c are fitted values based on the measured data. The electrical resistance of power trip for the test tube , $(R_T)_{TRIP}$, is obtained by substituting the power trip temperature, $\overline{T}_{TRIP}$, into Eq. (62).

$$(R_T)_{TRIP} = a(1 + b\overline{T}_{TRIP} + c\overline{T}^2_{TRIP}) \tag{63}$$

The schematic of a double bridge circuit is shown in Fig. 4. The current, I, through the standard resistance, R_s, can be regarded as that through the test tube. Therefore the heat

generation of the test tube, Q, is expressed by the following form. The current at the power trip temperature, I_{TRIP}, is calculated.

$$Q = I^2 (R_T)_{TRIP} = Q_v \frac{\pi\{(d+2\delta)^2 - d^2\}L}{4} \tag{64}$$

$$I_{TRIP} = \sqrt{Q_v \frac{\pi\{(d+2\delta)^2 - d^2\}L}{4(R_T)_{TRIP}}} \tag{65}$$

where Q_v is the heat input per unit volume (W/m^3). The double bridge circuit is balanced for small current at a liquid temperature. When the direct current is supplied to the test tube, the electrical resistance of the test tube increases. As a result, the unbalance voltage, V_T, is expressed by means of Ohm's low. The power trip voltage, $(V_T)_{TRIP}$, at the power trip temperature is calculated as the following form.

$$(V_T)_{TRIP} = \frac{I\{(R_T)_{TRIP} \times R_2 - R_1 \times R_3\}}{R_2 + R_3} \tag{66}$$

The value of $(V_T)_{TRIP}$ is given the comparator of the heat input control block in Fig. 4 as the preset temperature to avoid test tube damage. This procedure avoids actual burnout of the test tube.

A.3. Numerical solutions of RANS Equations for k-ε Turbulence Model with Low Reynolds Number Form

Figure 20 shows the typical example of the steady-state turbulent heat transfer curve (black solid line) for Pt circular tube of d=6 mm and L=69.6 mm with τ=22.5 s at u=13.51 m/s. The experimental data were compared with the values derived from authors' correlation of the steady-state turbulent heat transfer for the empty tube, Eq. (43) [16]. The heat fluxes gradually become higher with an increase in ΔT_L on the steady-state turbulent heat transfer curve derived from Eq. (43). The numerical solutions of the steady RANS equations for k-ε

turbulence model with the low Reynolds number form for the relation between q and ΔT_L are shown for q ranging from 1×10^5 to 2×10^7 W/m^2 at the outer control volume width on the r-component, $(\Delta r)_{out}$, of 1.62 μm as blue solid triangles. The 10 different values for the numerical solutions are plotted for the ΔT_L ranging from 0.32 to 60.12 K on the log-log graph. These solutions become also higher with an increase in the ΔT_L on the higher curve parallel to the steady-state turbulent heat transfer one derived from Eq. (43). The numerical solutions at the high heat flux point are 468.5 % higher than the experimental data at a fixed temperature difference between average inner surface temperature and liquid bulk mean temperature (ΔT_L=constant), and 180 K lower than the experimental data at a fixed heat flux (q=constant). And those of the unsteady RANS equations for k-ε turbulence model with the low Reynolds number form are shown for the q ranging from 2.55×10^5 to 1.01×10^7 W/m^2 at the $(\Delta r)_{out}$ of 1.36 and 1.62 μm as red and green solid triangles, respectively. The 14 and 14 different values for the numerical solutions are plotted for the ΔT_L ranging from 1.33 to 108.12 K on the log-log graph. Those are scattered and cannot also fit in the experimental data with. The thickness of the conductive sub-layer, δ_{CSL}, would not be precisely established from those steady-state turbulent heat transfer curves.

Then, the authors have supposed that the conductive sub-layer exists on the test tube surface and the liquid temperature in the conductive sub-layer on the test tube surface will become linearly lower with a decrease in the radius by the heat conduction from the surface temperature on the test tube, $T_f=T_s-\Delta rq/\lambda_l$ [14, 15]. And let those, T_f, equal the calculated liquid temperature of the outer control volume on the test tube surface, *TEM*, in the turbulent flow region, which is located on the center of the outer control volume as given in Eq. (42). Half the outer control volume width for the r-component, $(\Delta r)_{out}/2$, would become the

thickness of the conductive sub-layer, δ_{CSL}, for the turbulent heat transfer in a circular tube under two-phase model classified into conductive sub-layer and inner region of the turbulent flow [24]. The unsteady RANS equations for k-ε turbulence model with the high Reynolds number form have been numerically solved at $(\Delta r)_{out}$=13.04 μm and the numerical solutions for the relation between q and ΔT_L are shown for the q ranging from 2.55×10^5 to 8.49×10^6 W/m^2 in Fig. 20 as black solid circles. The 13 different values for the numerical solutions are plotted for the ΔT_L ranging from 3.71 to 119.11 K. These solutions become also higher with an increase in the ΔT_L along the curve derived from Eq. (43). These numerical solutions can be in good agreement with the experimental data and the values derived from Eq. (43) within ±10 % differences. The $(\Delta r)_{out}$ was given with 13.04 μm and the thickness of the conductive sub-layer, δ_{CSL}, of this steady-state turbulent heat transfer curve is established with 6.52 μm.

Table 1 The values of the constants in the Chen-Kim k-ε turbulence model [11].

σ_k	σ_ε	σ_t	C_{1e}	C_{2e}	C_{3e}	C_μ
0.75	1.3	1.0	1.15	1.9	0.25	0.5478

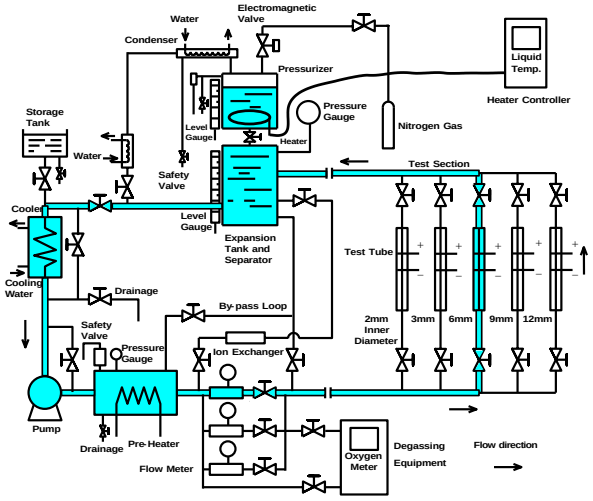

Fig. 1 Schematic diagram of experimental water loop.

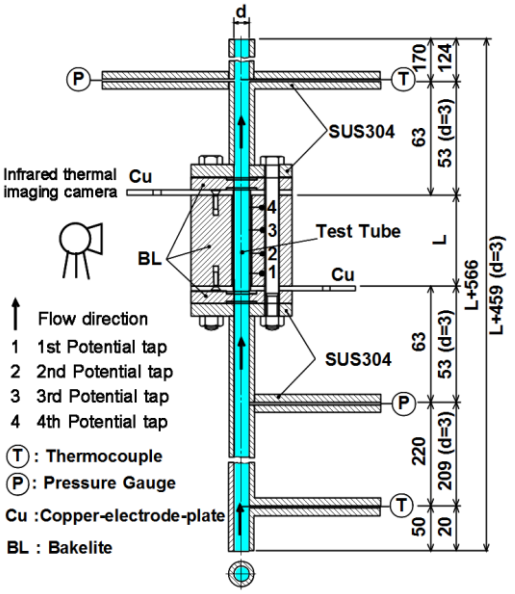

Fig. 2 Vertical cross-sectional view of 6-mm inner diameter test section.

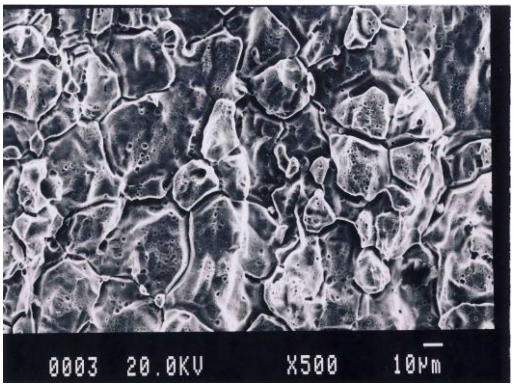

Fig. 3 SEM photograph for the SUS304 test tube of *d*=6 mm with the rough finished inner surface.

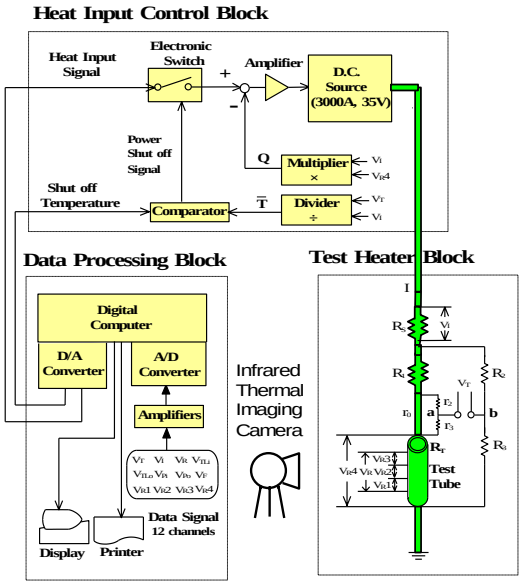

Fig. 4 Measurement and data processing system.

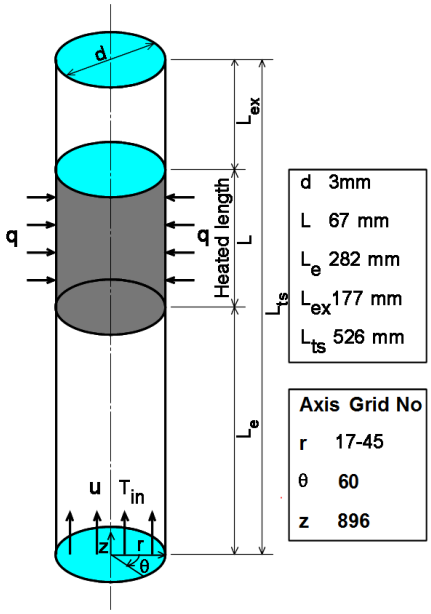

Fig. 5 Physical model for numerical analysis.

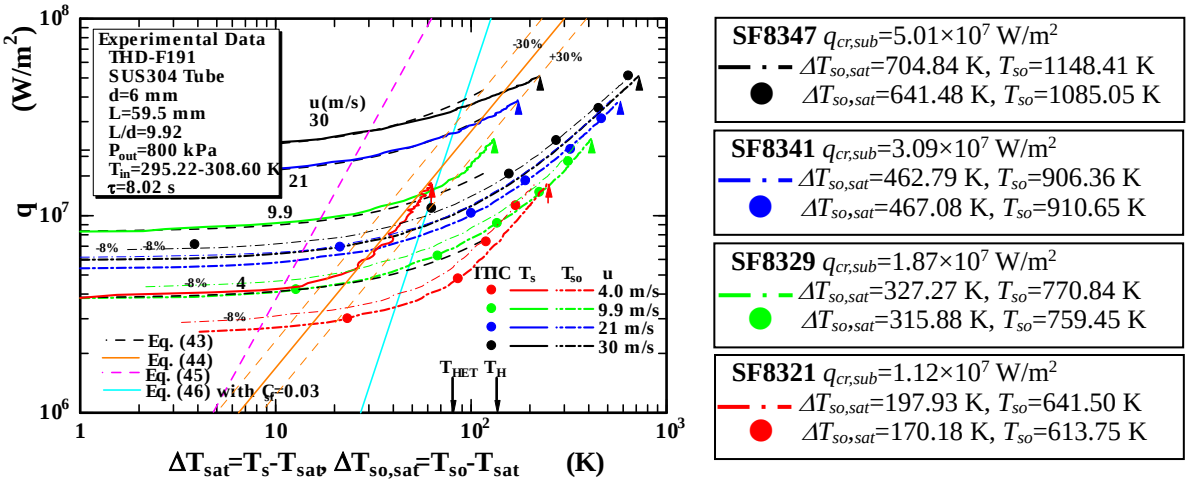

Fig. 6 Typical heat transfer processes on the THD-F191 SUS304 test tube of d=6 mm and L=59.5 mm with the rough finished inner surface for τ=around 8.02 s with u=4 to 30 m/s, outer surface temperatures of the test tube calculated from Eq. (13) and observed by an infrared thermal imaging camera (ITIC).

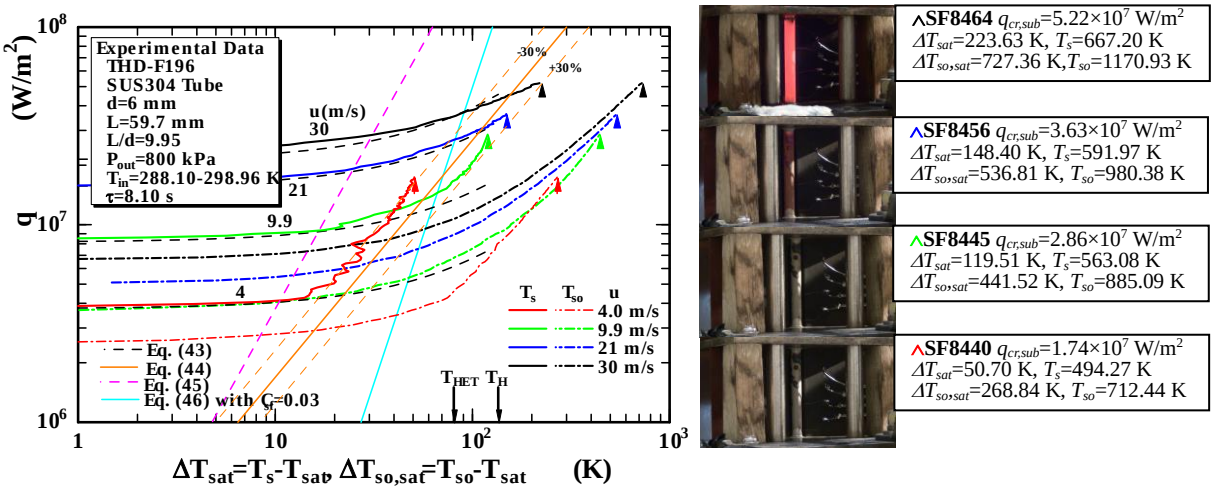

Fig. 7 Typical heat transfer processes on the THD-F196 SUS304 test tube of d=6 mm and L=59.5 mm with the rough finished inner surface for τ=around 8.10 s with u=4 to 30 m/s, outer surface temperatures of the test tube calculated from Eq. (13) and the color temperatures of outer surface of the test tube observed by a video camera (VC).

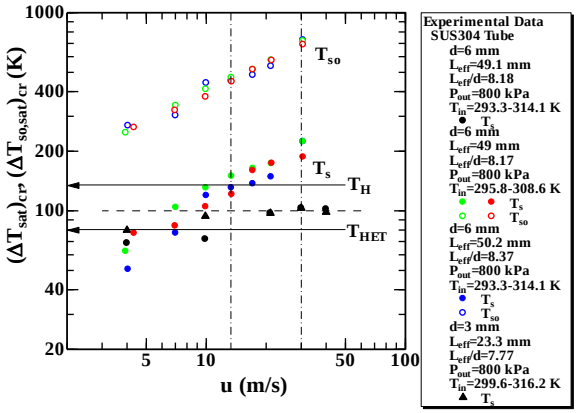

Fig. 8 Values of ΔT_{sat} and $\Delta T_{so,sat}$ at CHF points ($(\Delta T_{sat})_{cr}$ and $(\Delta T_{so,sat})_{cr}$) versus u for Vertical SUS304 test tubes of d=3 and 6 mm.

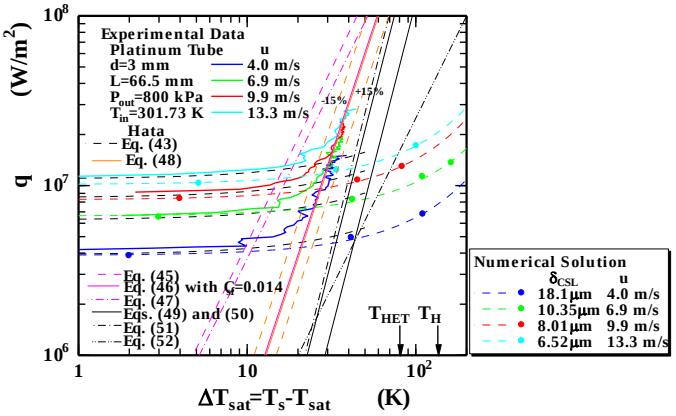

Fig. 9 Typical heat transfer processes on the Pt test tube of d=3 mm and L=66.5 mm for τ=around 8 s with u=4.0, 6.9, 9.9 and 13.3 m/s compared with numerical solutions of inner surface temperature [4].

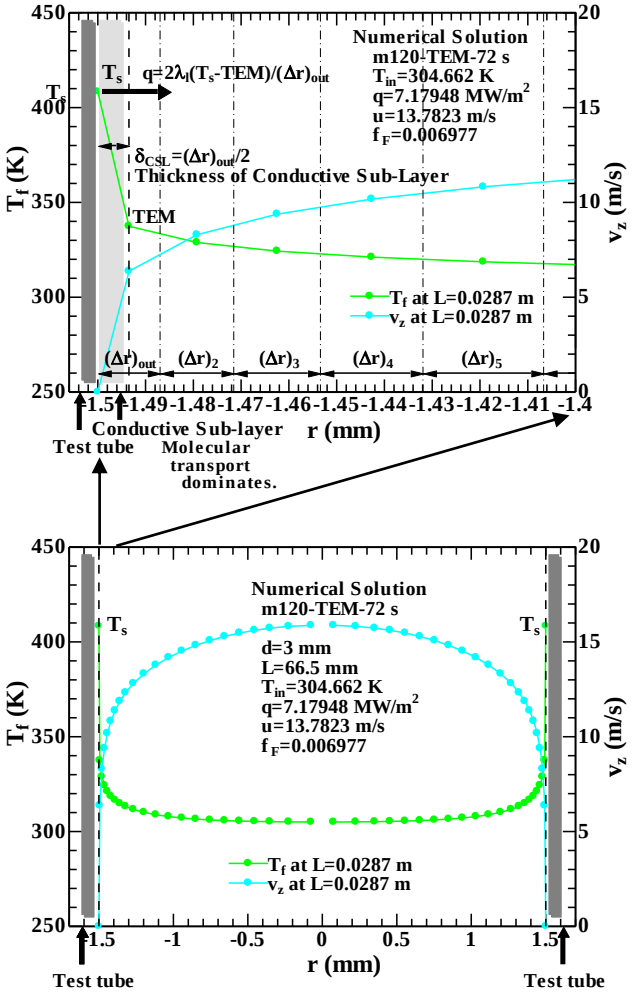

Fig. 10 Liquid temperatures in the conductive sub-layer, δ_{CSL}, based on numerically predicted data points (solution of RANS equations) for d=3 mm test tube.

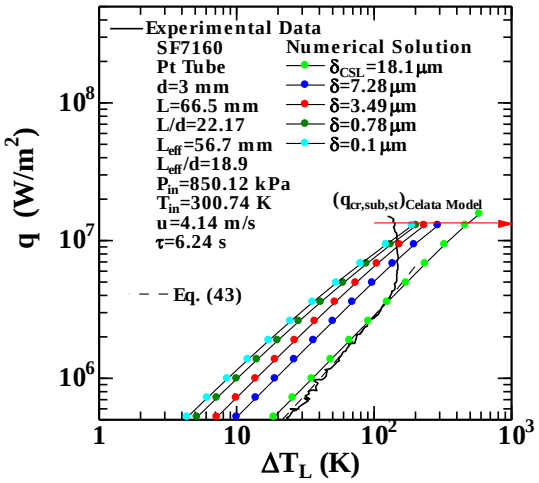

Fig. 11 Heat transfer process on the Pt test tube of d=3 mm and L=66.5 mm for τ=6.24 s with u=4.14 m/s compared with heat transfer curves numerically analyzed by δ_{CSL}, δ=18.1 to 0.1 μm.

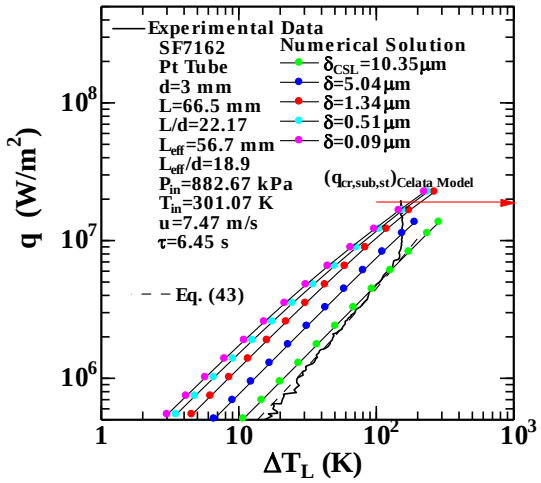

Fig. 12 Heat transfer process on the Pt test tube of d=3 mm and L=66.5 mm for τ=6.45 s with u=7.47 m/s compared with heat transfer curves numerically analyzed by δ_{CSL}, δ=10.35 to 0.09 μm.

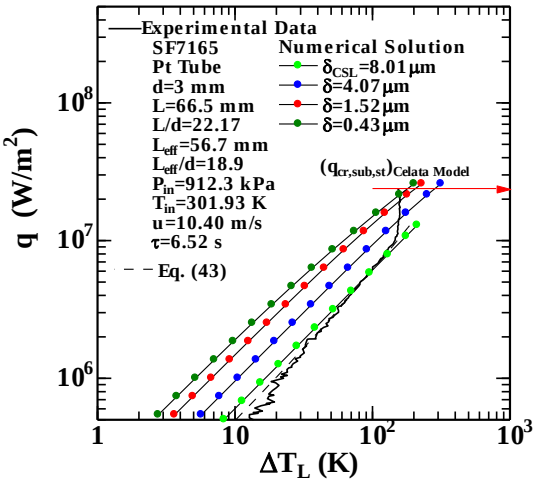

Fig. 13 Heat transfer process on the Pt test tube of d=3 mm and L=66.5 mm for τ=6.52 s with u=10.40 m/s compared with heat transfer curves numerically analyzed by δ_{CSL}, δ=8.01 to 0.43 μm.

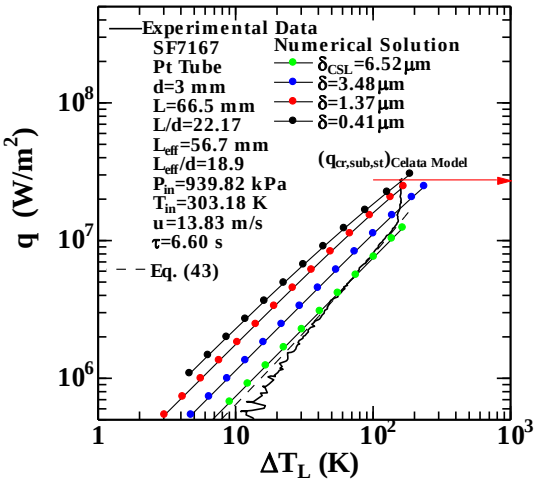

Fig. 14 Heat transfer process on the Pt test tube of d=3 mm and L=66.5 mm for τ=6.60 s with u=13.83 m/s compared with heat transfer curves numerically analyzed by δ_{CSL}, δ=6.52 to 0.41 μm.

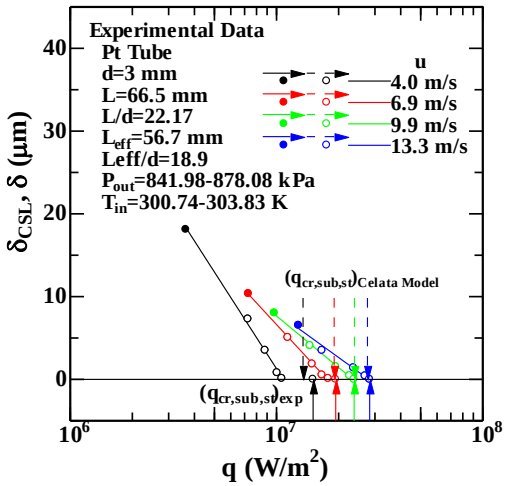

Fig. 15 Experimentally measured thicknesses of the conductive sub-layer on forced convection and nucleate boiling heat transfer, δ_{CSL} and δ, versus heat flux for Pt test tube of d=3 mm with u=4 to 13.3 m/s.

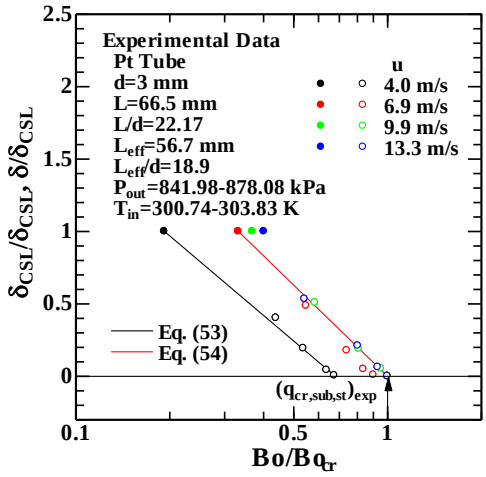

Fig. 16 Relationship between $\delta_{CSL}/\delta_{CSL}$, δ/δ_{CSL} and Bo/Bo_{cr} for Pt test tube of d=3 mm with u=4 to 13.3 m/s.

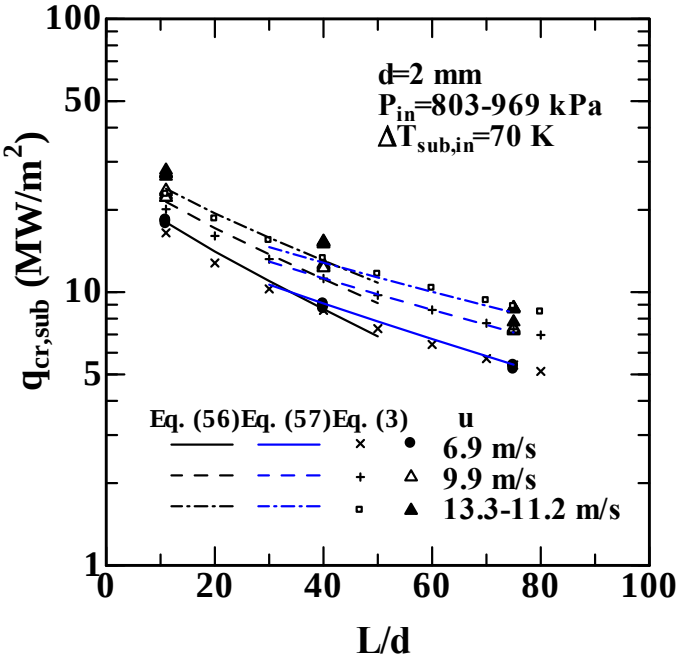

Fig. 17 $q_{cr,sub}$ vs. L/d for an inner diameter of 2 mm at $\Delta T_{sub,in}$ of 70 K with the flow velocity of 6.9, 9.9 and 13.3 m/s.

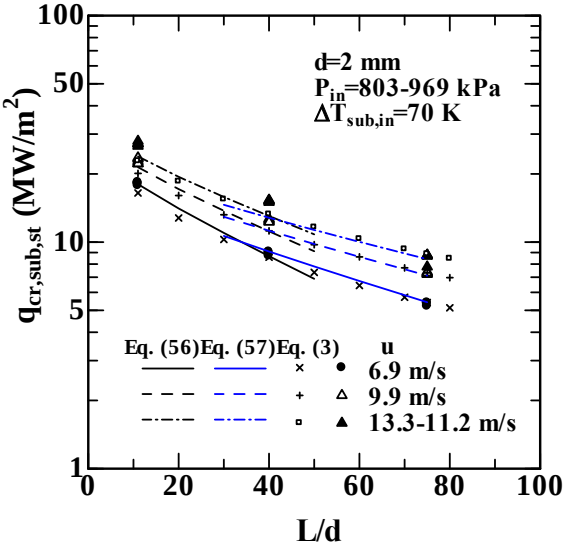

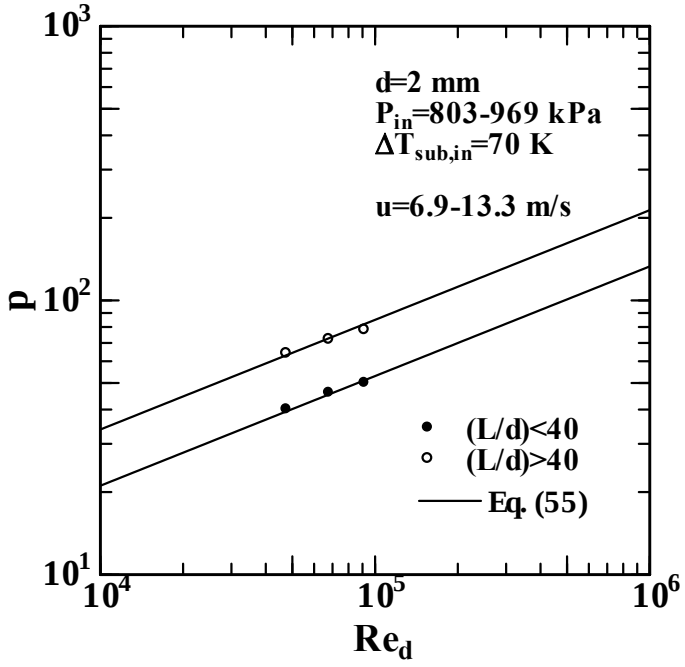

Fig. 18 *p* vs. Re_d for an inner diameter of 2 mm at $\Delta T_{sub,in}$ of 70 K with the flow velocity of 6.9, 9.9 and 13.3 m/s.

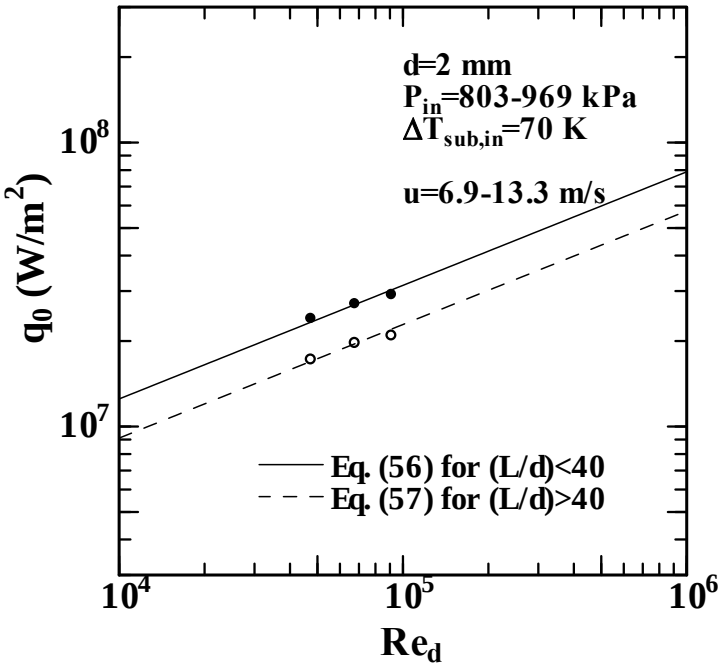

Fig. 19 q_0 vs. Re_d for an inner diameter of 2 mm at $\Delta T_{sub,in}$ of 70 K with the flow velocity of 6.9, 9.9 and 13.3 m/s.

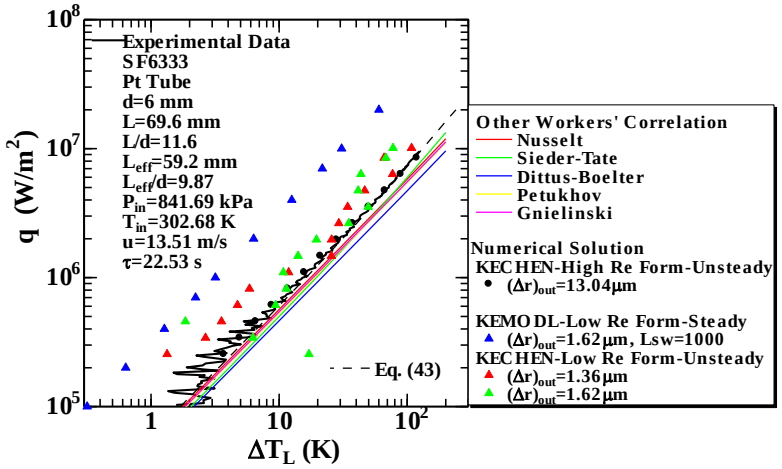

Fig. 20 Relationship between q and ΔT_L for circular tube of d=6 mm and L_{eff}=59.2 mm compared with theoretical equations for k-ε turbulence model with the low Reynolds number form.